Modeling upwelling circulation off the Oregon coast

Jianping Gan

Department of Mathematics and Atmospheric, Marine and Coastal Environment Program, Hong Kong University of Science and Technology, Kowloon, Hong Kong

J. S. Allen

College of Oceanic and Atmospheric Sciences, Oregon State University, Corvallis, Oregon, USA

Received 1 September 2004; revised 20 April 2005; accepted 17 July 2005; published 20 October 2005.

[1] Time-dependent, three-dimensional, upwelling circulation on the continental shelf off the Oregon coast is studied using a primitive equation numerical model. A limited area domain with a high-resolution curvilinear grid is utilized. The response of the coastal ocean to forcing by observed wind stress and heat flux during the summer 2001 time period of the Coastal Ocean Advances in Shelf Transport (COAST) field experiment is investigated. Model results are compared to COAST current and hydrographic measurements. The shelf velocity and density fields are generally characterized by the presence of a southward alongshore coastal jet with an upwelling density front on the shoreward side of the jet. The large variability in shelf topography associated with Heceta Bank exerts a major influence on the shelf velocity and density fields. Over the bank the alongshore coastal jet is displaced offshore, and colder upwelled water extends farther from the coast. Northward mean flow and upward motion are found inshore of the jet. Three-dimensional flow structures in response to variable shelf bottom topography are presented, and an analysis of time- and space-dependent alongshore momentum balances is applied to clarify the associated dynamics. In general, northward pressure gradients, set up over the bank during southward upwelling winds, accelerate currents on the inshore side of the jet northward when the winds relax. Analysis of term balances in the depth-averaged equation for potential temperature shows that during upwelling, across-shore advection makes the major contribution to cooling over most of the region, except inshore over Heceta Bank, where alongshore advection also plays a significant role.

Citation: Gan, J., and J. S. Allen (2005), Modeling upwelling circulation off the Oregon coast, *J. Geophys. Res.*, *110*, C10S07, doi:10.1029/2004JC002692.

1. Introduction

[2] During summer, prevailing southward winds produce strong upwelling and an associated southward coastal jet over the continental shelf off Oregon. The upwelling circulation forms cold and nutrient-rich surface waters near the coast. Along the north central part of the Oregon coast between 45°N and 45.5°N, relatively uniform bottom topography in the alongshore direction (Figure 1) generally leads to the prototypical upwelling situation with formation of colder surface water and a southward alongshore coastal jet next to the coast. Over the central Oregon shelf between 43.5°N and 45°N, the highly variable bottom topography over Heceta Bank has a significant influence on the upwelling flow field. A complex three-dimensional flow pattern with offshore shifting of the coastal jet and development of northward flow on the inshore side of the jet is found over the bank [*Oke et al.*, 2002a, 2002b; *Gan et al.*, 2005; *Kurapov et al.*, 2005a, 2005b; *Castelao and Barth*, 2005; *Kosro*, 2005]. Along the southern part of the Oregon coast between 42°N and 43°N, an enhancement of upwelling, jet separation and eddy formation are found to be related to interactions of the wind-forced coastal currents with Cape Blanco [*Barth et al.*, 2000]. The dynamical importance of coastline and bottom topography on the wind-forced coastal flow off northern California was demonstrated in model experiments by *Gan and Allen* [2002a, 2002b]. In addition to topographic effects, alongshore variations in coastal circulation may also be caused by spatial variations of the wind field along the coast. *Gan et al.* [2005] applied a space-varying wind stress obtained from a mesoscale atmospheric model [*Samelson et al.*, 2002] to a limited area coastal model off Oregon and found considerable spatial variability of upwelling along the Oregon coast in response to the general increase in magnitude of the wind stress to the south. The dynamical processes involved in the complex variability of the three-dimensional flow fields off Oregon, subject to the controls of both wind and topography variations, are not well understood.

[3] Coastal Ocean Advances in Shelf Transport (COAST) is a multidisciplinary research project designed to understand ecosystem dynamics in the wind-driven coastal cir-

0148-0227/05/2004JC002692$09.00

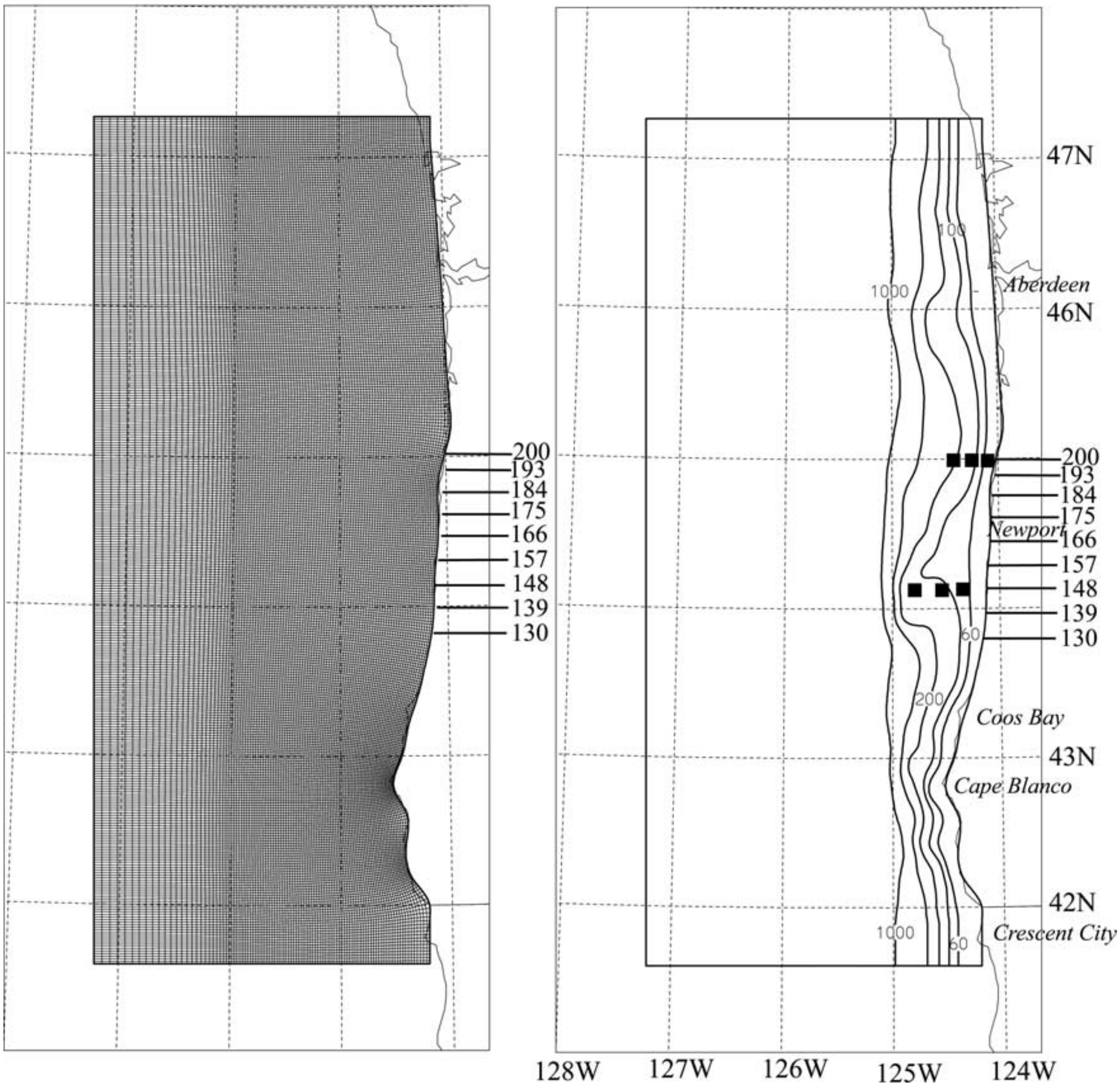

Figure 1. Model curvilinear grid and bathymetry with the 60, 100, 200, 500, and 1000 m isobaths shown. The horizontal grid spacing ranges from 1.5 km near the coast to 6 km offshore, with 45 vertical sigma levels. The grid extends about 633 km alongshore and 250 km across-shore and contains three open boundaries. The locations of moorings are marked with solid squares, and the locations of across-shore sections are labeled with their alongshore grid numbers. The COAST meteorological buoy is located near the midshelf mooring of the 45°N line.

culation on the continental shelf off the Oregon coast. The objective of the present study is to develop and apply a physical modeling capability to help understand the dynamics of the observed flow field. In particular, we investigate the dynamical mechanisms associated with alongshore variations in the three-dimensional circulation in the general region of the COAST field experiment between 43.7°N and 45°N during summer 2001. That region includes the relatively alongshore uniform shelf to the north near 45°N as well as the more complex topographic variability around Heceta Bank near 44°N. In a companion paper [*Spitz et al.*, 2005], the corresponding behavior of the Oregon coastal ecosystem is studied for the same time period using the same physical model.

[4] The outline of the paper is as follows. The ocean model and its implementation are introduced in section 2. Comparisons of model results and observations are given in section 3. The characteristics of the time-averaged three dimensional flow field are described in section 4. Analyses of time-averaged and time-dependent depth-averaged and depth-dependent alongshore momentum balances are discussed in section 5. Features that occur during a 10 day period containing intervals of northward, downwelling-favorable winds are analyzed and compared with conditions during a 10 day period of sustained southward, upwelling-favorable winds in section 6. A summary is given in section 7.

2. Ocean Model

[5] The model used is the Princeton Ocean Model (POM) [*Blumberg and Mellor*, 1987] for three-dimensional, time-

dependent, oceanographic flows governed by the hydrostatic primitive equations. The model incorporates the level 2.5 turbulent closure scheme of *Mellor and Yamada* [1982] to parameterize small-scale vertical mixing. The model domain extends alongshore 634 km, from 41.7°N to about 47.3°N, and offshore 250 km with the coastline boundary fitted by a curvilinear coordinate (Figure 1). The numbers of grid points in the (x, y, σ) directions are (101, 323, 45) where (x, y) are aligned in the across-shore (positive toward the east) and alongshore (positive toward the north) directions, respectively. The horizontal grid spacing is variable, with minimum spacing near the coast ($\triangle x$ = 1.5 km, $\triangle y$ = 1–2 km) and a larger grid size in x ($\triangle x$ = 6 km) in the western part of the domain (Figure 1). The alongshore direction of the offshore boundary has been rotated 0.2° counterclockwise from north so as to be better aligned with the coastline. The model domain contains three open boundaries on the north, south and west, respectively. In this study, periodic boundary conditions are chosen in the alongshore direction. This choice helps provide a well-posed numerical problem and avoids use of approximate open boundary conditions on the north and south boundaries that might be particularly troublesome for the closely related ecosystem modeling study of *Spitz et al.* [2005]. For limited time integrations of wind-forced shelf flows dominated by local flow topography interactions, the errors introduced by periodic boundary conditions appear, based on model-data comparisons, to be acceptable, particularly over the inner shelf [*Gan and Allen*, 2002b; *Oke et al.*, 2002a]. Thus we feel that the robust features of the mesoscale physical circulation processes for the central Oregon shelf will be adequately represented with the present model domain. We readily acknowledge, however, that additional research is needed to determine optimum methods for effective implementation of high-resolution coastal circulation models. On the western open boundary, the normal component of the depth-integrated velocity is set to zero. An Orlanski-type radiation boundary condition is applied to the depth-dependent velocity components, to the tangential component of the depth-integrated velocity, and to the temperature and salinity. A no gradient condition is used for the surface elevation. Realistic continental shelf and bottom topography off Oregon is utilized. In order to apply periodic boundary conditions, regions with straight coastline of alongshore extent 10 km north of 47°N and 33 km south of 42°N are added. The bottom topography is adjusted gradually so that it agrees at the north and south boundaries. Since the study is focused mainly on the flow field over the continental shelf, the maximum water depth is chosen to be 1200 m so that a larger barotropic time step can be used.

[6] The model is initialized with zero velocities and with horizontally uniform temperature and salinity profiles obtained from June climatological values at a station 25 nautical miles off Newport (Figure 1). Wind measurements from the COAST meteorological buoy at 45°N and from the NDBC buoy at 44.6°N (Figure 2) are used to calculate wind stress following *Large and Pond* [1981]. The wind stress is assumed to be spatially uniform. Since the behavior of subinertial frequency flow is to be investigated in the study, the time series of wind stress (Figure 2) is filtered with a 36 hour low-pass filter. The surface heat flux is obtained from bulk aerodynamic formulae as described by *Gan and Allen* [2002b] using meteorological observations from the COAST meteorological buoy. The horizontal kinematic eddy viscosity and diffusivity coefficients are constant and chosen to be small 10 m^{2}s^{-1}.

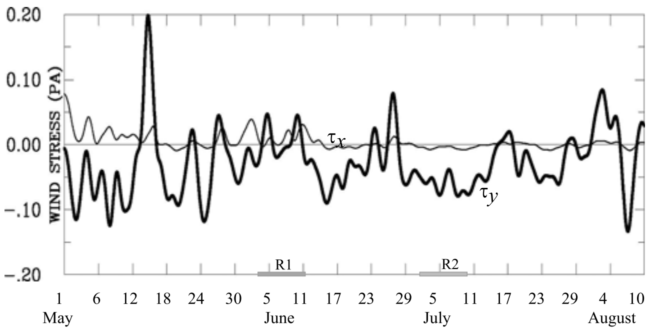

Figure 2. Time series of wind stress components calculated from wind measurements at the COAST meteorological buoy (45°N, 80 m water depth) and, for 1–16 May, at the NDBC buoy (44.6°N, 130 m water depth). The heavy line is the alongshore component (positive northward), and the light line is the across-shore component (positive eastward). Two 10 day time periods dominated by northward wind forcing (R1, 3–12 June) and by southward wind forcing (R2, 1–10 July) are indicated in the figure. The mean values and standard deviation of (τ_x, τ_y) are (0.004,−0.029) Pa and (0.012,0.050) Pa, respectively.

[7] The simulation is started on 1 May and forced for 102 days to 10 August. The first 22 days are regarded as a spin-up period. The model results from the following 72 days from 23 May to 2 August are used for most of the analysis. Some observations and model time series (Figures 3 and 4) are compared for 80 days from 23 May to 10 August.

3. Comparisons With Observations

[8] During summer 2001 from late May to late August, six current meter moorings were deployed on two east-west lines across the shelf in the north at 45°N and in the south at 44.2°N. There are three moorings on each line (Figure 1), deployed at locations on the inner shelf (50 m water depth), midshelf (80 m in the north; 90 m in the south) and shelf break (130 m) [*Boyd et al.*, 2002]. High-resolution CTD surveys were conducted during two periods, one in May–June and the another in July–August [*Barth et al.*, 2003]. Detailed descriptions of the field experiment can be found in the related papers collected in this volume [e.g., *Castelao and Barth*, 2005]. Related modeling studies for summer 2001 involving assimilation of the velocity measurements from the COAST moored current meter moorings are described by *Kurapov et al.* [2005a, 2005b].

[9] Time series of model and observed depth-averaged alongshore velocity from the six mooring locations are filtered by averaging over an inertial period which removes high-frequency fluctuations associated with inertial oscillation and the semidiurnal tide (Figure 3). Corresponding time series of potential temperature at near surface and near bottom locations are shown in Figure 4. Correlation coef-

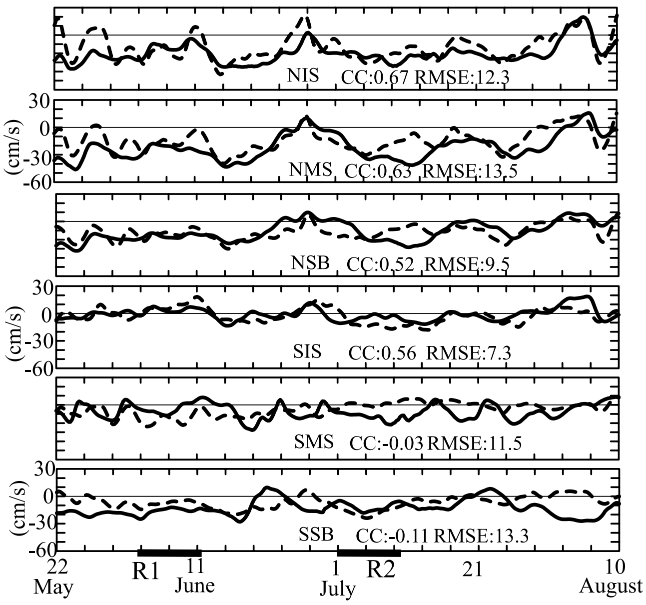

Figure 3. Time series of observed (dashed lines [*Boyd et al.*, 2002]) and modeled (solid lines) inertially averaged alongshore depth-averaged velocities (cm s^{-1}) for inshore (NIS), midshelf (NMS), and shelf break (NSB) moorings along the northern line and for the inshore (SIS), midshelf (SMS), and shelf break (SSB) moorings along the southern line. Correlation coefficients (CC) and root mean square error (RMSE) between corresponding observed and modeled velocities are listed. The time periods R1 and R2 are marked.

ficients (CC) and the root mean square errors (RMSE) between the corresponding observations and model variables are also given in Figures 3 and 4. Both model results and measurements indicate dominantly southward alongshore currents at the north line where the bottom topography is relatively uniform in the alongshore direction. Model and observed depth-averaged currents are reasonably well correlated, with larger CCs ranging from 0.52 to 0.67 found at the moorings on the north line and at the inner shelf mooring of the south line, indicating that the time variability of the flow associated with the wind forcing is fairly well captured by the model at those locations. At the midshelf and shelf break moorings of the south line, however, the CC values are low, while the RMSE values are similar to those found on the north line. The analyses of the model results that follow show that the flow in the southern region over Heceta Bank is characterized by more complex time- and space-dependent variability than in the north. Evidently the mesoscale variability in that region is more turbulent and is not well represented deterministically by the model. Similar behavior was found in the data assimilation study of *Kurapov et al.* [2005a] where, for the time period 26 May to 10 July 2001, comparatively low RMSE and high CC values at the southern midshelf mooring SMS were obtained only with assimilation of the current measurements from SMS and SSB. That assimilation solution resulted, for example, in a quantitative, but not qualitative, change in the location and alignment of the mean coastal jet along the southern mooring line [see *Kurapov et al.*, 2005a, Figure 3]. In addition, generally larger southward currents are found in the model results and the magnitude of northward currents in some of the events related to the relaxation of upwelling favorable wind stress are underestimated by the model.

[10] It should be noted that the effects from much stronger winds south of Heceta Bank [*Samelson et al.*, 2002; *Gan et al.*, 2005] and a possible northward pressure gradient force as part of the interior ocean response over larger alongshore scales are not included in the present study. Nevertheless, overall the reasonably good time-dependent performance of the model currents along the north line and at the inshore location of the south line, together with the similar RMSE values at the midshelf and shelf break moorings in the south, provide confidence in the use of the model solutions for the analysis of dominant dynamical processes associated with local flow topography interactions.

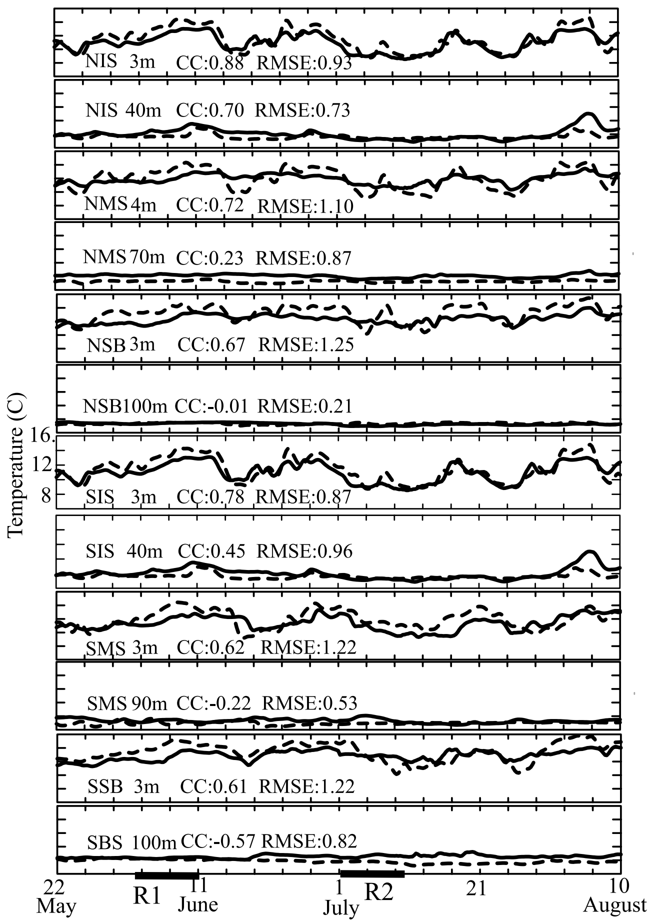

Figure 4. Time series of observed (dashed lines [*Boyd et al.*, 2002]) and modeled (solid lines) inertially averaged water temperature (°C) at near-surface and near-bottom depths for the inshore (NIS), midshelf (NMS), and shelf break (NSB) moorings along the northern line and for the inshore (SIS), midshelf (SMS), and shelf break (SSB) moorings along the southern line. Correlation coefficients (CC) and root mean square error (RMSE) between corresponding observed and modeled temperatures are listed. The time periods R1 and R2 are marked.

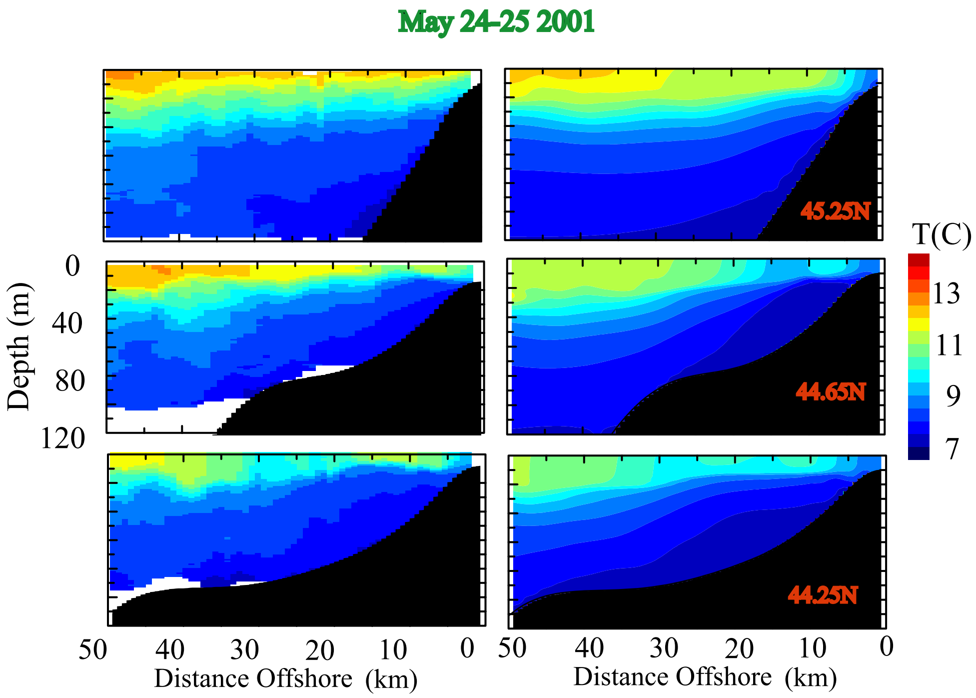

Figure 5. Across-shore sections of (left) observed [*Barth et al.*, 2003] and (right) modeled temperature at lines 45.25°N, 44.65°N, and 44.25°N on 24–25 May 2001.

[11] A comparison of model and observed temperatures shows fairly good agreement overall (Figure 4). In general, larger CCs are found near the surface. At the midshelf and shelf break moorings on the southern line, the CCs for near-surface temperatures are high even though the CCs are very low for the corresponding depth-averaged alongshore velocity (Figure 3). The generally small values of RMSE at all moorings from the temperature comparisons indicate that the thermal field of the model is close to the conditions in the ocean.

[12] The agreement between modeled and observed results can also be seen from a comparison (Figure 5) of across-shore sections of temperature at 45.25°N, 44.65°N (Newport) and 44.25°N (Heceta Bank) [*Barth et al.*, 2003] on 24–25 May during upwelling favorable winds. Although, the near surface modeled temperatures appear to be slightly colder than the observed, a feature that is visible also from the time series in Figure 4, the intensity and the structure of the upwelled temperature fields appear to be similar. Upwelled colder waters with temperature of about 8°–9°C are found at the surface within 5 km of the coast and warmer surface waters of about 14°C are located offshore in both the model solution and in the measurements.

[13] The effect of the variable bottom topography associated with Heceta Bank on the thermal field is clearly visible in a comparison of model and observed horizontal temperature fields at 15 m depth on 26 May (Figure 6), during a period of relaxation of upwelling winds [see also *Castelao and Barth*, 2005]. The coldest water is found over the east side of the bank close to coast. In the model, at the southern tip of the bank a northward current associated with the effect of local topography has advected warmer surface water northward. During periods of relaxation of upwelling favorable wind, the shelf flow response results in a strengthened northward flow over the inner part of the bank as will be discussed later in the paper. The corresponding response of the model temperature field to the northward flow is shown by a region of lower temperature located over the bank around 44°N. A qualitatively similar structure may be seen in the observed field.

4. Time Mean Circulation

[14] Fields of time mean surface velocity vectors, surface temperature, their associated standard deviations (std) and fields of mean surface elevation and vorticity during the period from 23 May to 2 August (Figures 7 and 8) show the shelf flow response to the dominant southward upwelling winds. A southward coastal jet, mostly paralleling the coastline except over the Heceta Bank, is present over the shelf. The flow field is markedly altered by the presence of Heceta Bank (44°N) as well as the coastline geometry around Cape Blanco (42.8°N). The shallowing of the shelf topography associated with Heceta Bank and the variation of coastline curvature provided by Cape Blanco result in an offshore veering of the jet at these locations and exert a major influence on the shelf circulation pattern. The jet shifts offshore south of 45°N following the orientation of the bottom isobaths as it encounters the shallower shelf near Heceta Bank. At the southern edge of Heceta Bank, the jet turns shoreward forming a region of positive vorticity (Figure 8a) south of the bank. Strong temporal variability of the surface velocity field (Figure 7b) occurs in this region over and south of Heceta Bank and is also found on the nearshore edge of the jet along the coast and south of Cape Blanco. We note that the spatial structures of the model

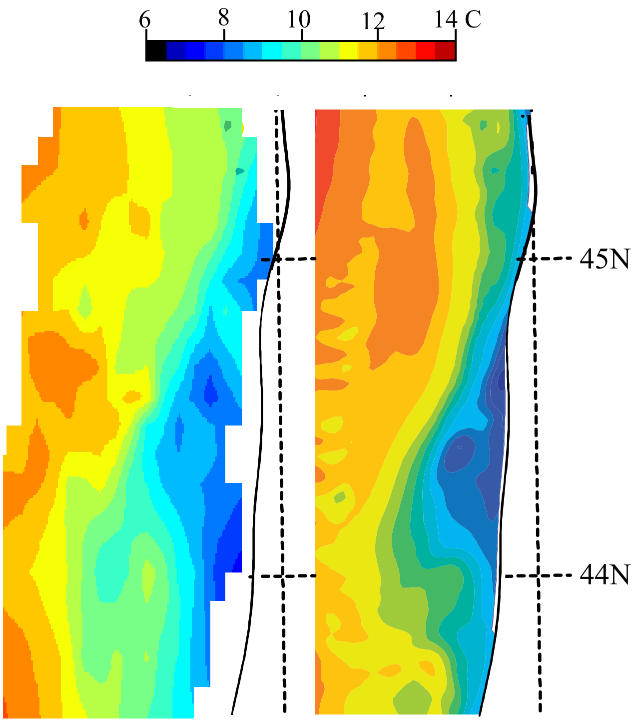

Figure 6. (left) Observed [*Barth et al.*, 2003] and (right) modeled water temperature at 15 m depth during upwelling on 26 May 2001.

time mean surface velocity vectors and standard deviation (Figures 7a and 7b) are in very good agreement with those calculated for April–September 2001 from HF radar surface current measurements between 44.2°N and 45°N [see *Kosro*, 2005, Figure 7]. Relatively low mean values and large variability of the model surface temperatures also exist in this general location (Figures 8b and 8c) reflecting the substantial influence of Heceta Bank on the upwelling circulation. The time- and space-dependent dynamical processes involved in these time-averaged responses will be analyzed in the following sections.

[15] The fields of time mean bottom velocity vectors, bottom density and twice the turbulent kinetic energy q^2 at the bottom are shown in Figure 9. The onshore currents at the bottom near the coast, particularly visible around 45°N, generally reflect onshore flow in a bottom Ekman layer contributing to the upwelling circulation in response to the time mean offshore surface Ekman transport. Relatively large magnitude onshore and southward bottom velocities also exist under the coastal jet offshore over Heceta Bank. South of the central part of Heceta Bank, the mean bottom velocities are northward. These northward bottom currents evidently advect relatively high-density bottom water northward over the bank (Figure 9b). Relatively strong bottom turbulent kinetic energy is found within the core of the jet near the coast from 44.6°N to 45.5°N and offshore over Heceta Bank from 44°N to 44.6°N consistent with the bottom velocity field and bottom boundary layer dynamics. The bottom density field also shows the results of advection of relatively less dense water on the outer southern part of Heceta Bank.

[16] The alongshore variations of the time mean three-dimensional flow and density fields are shown in Figure 10 by across-shore sections of the alongshore velocity v, vertical velocity w, and potential density σ_θ at a set of different locations along the coast denoted by their alongshore grid numbers marked in Figure 1. At line 200, where the shelf topography is relatively uniform in the alongshore direction, the time mean coastal jet is trapped within about 20 km from the shore. The jet has a maximum magnitude of about 1 ms^{-1}. Velocities of magnitude 0.15 ms^{-1} extend vertically to a depth of about 60 m. As the jet travels south past line 184, it gradually veers offshore following the offshore direction of the bottom isobaths. The mean coastal jet reaches the farthest offshore location (about 64 km offshore) at line 139, south of the bank, before moving shoreward. As it flows southward from line 200, the jet widens, the maximum magnitude of the velocities decrease, and the depth of appreciable magnitude currents, e.g., 0.15 ms^{-1}, increases. A northward mean current develops on the shoreward side of the jet starting near line 175 at Newport. The mean northward current reaches a maximum value at line 157 over the bank. Its across-shore extent continuously increases offshore from line 157 southward to line 130. Relatively strong horizontal shear of the alongshore velocity is found on the shoreward side of the jet although that shear weakens as the jet flows southward from line 175. The redevelopment of a southward coastal jet next to the coast, inshore of the mean northward current, starting at line 166 and gradually strengthening toward the south to line 130 is also evident.

[17] The spatial structure of the mean vertical velocity w is closely related to the alongshore and across-shore variations in v. At the northern lines 200 and 193, upward motion (positive w) is located mainly in the lower part of the water column with relatively large values close to the bottom. This reflects a typical coastal upwelling process where deeper

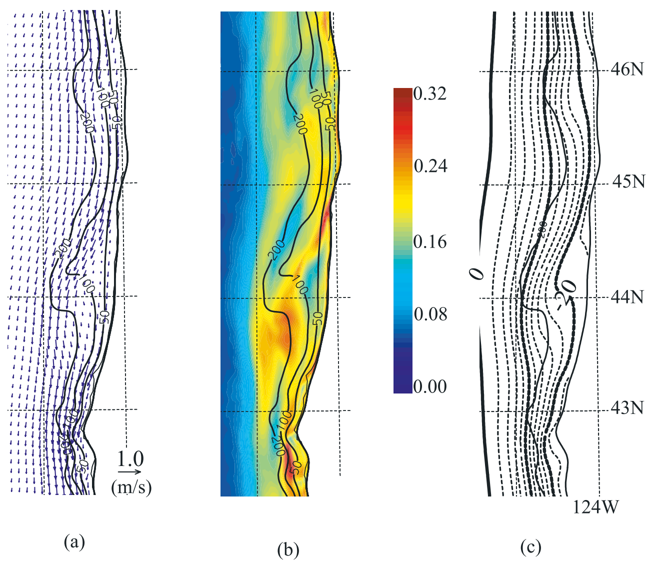

Figure 7. (a) Time mean surface velocity vectors (ms^{-1}), (b) standard deviation of the vector amplitudes (ms^{-1}), and (c) time mean surface elevation (cm) with contour intervals of 2 cm and heavy contour lines for −10 and −20 cm.

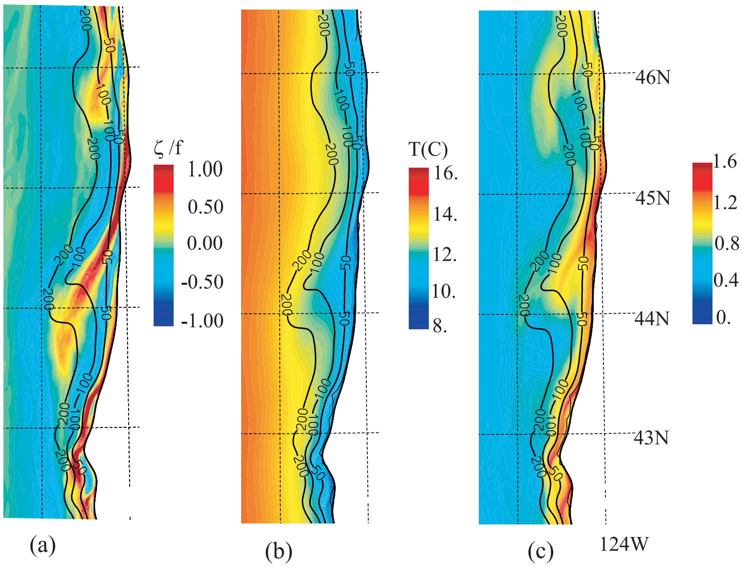

Figure 8. (a) Time mean surface vorticity divided by the Coriolis parameter f, (b) time mean surface temperature (°C), and (c) standard deviation of the surface temperature (°C).

bottom waters are advected shoreward and upward toward the coast with a substantial component of the onshore flow in a bottom Ekman layer. Over Heceta Bank, the structure of w changes markedly from that at the lines north of the bank. From line 175 to line 148, a downward velocity (negative w) develops in the water column of the jet core, with larger magnitudes near the bottom. This behavior is evidently related to the advection of the coastal jet offshore into regions of greater depth on the shelf.

[18] The region of negative vertical velocity w on the shelf from section 166 south is bounded by adjacent regions inshore and offshore with positive mean w. The regions with positive w on the inner shelf over the bank also contain positive onshore currents u (not shown) and are thus characterized by relatively strong shoreward and upward upwelling currents in the interior of the water column. The mean positive onshore currents over the inner shelf from section 166 south evidently provide the mass flux for the southward coastal jet that develops next to the coast and increases in strength toward the south.

[19] The potential density fields reflect the response to the three-dimensional upwelling circulation. North of the bank, the isopycnals generally slope upward toward the coast as deeper waters with relatively large potential density are upwelled to the surface. The density sections for the lines under the influence of the variable topography of the bank (148–175) are characterized by the existence of a pool of relatively high-density water at midshelf and by regions offshore of upward sloping isopycnals on the inshore side of the offshore displaced coastal jet.

5. Momentum Balances

[20] Analyses of momentum term balances are helpful for identifying the dynamical mechanisms that determine the wind-driven upwelling shelf flow response along highly variable shelf topography, as shown by *Gan and Allen* [2002a, 2002b].

[21] The depth-averaged and depth-dependent alongshore momentum equations from the model are given below in equations (1) and (2), respectively:

$$\overbrace{\frac{\partial V_b D}{\partial t}}^{1} + \overbrace{\frac{\partial U_b V_b D}{\partial x} + \frac{\partial V_b^2 D}{\partial y} - F_{by} - G_y}^{2} + \overbrace{fU_bD}^{3}\ \overbrace{-\tau_{ys}}^{4} + \overbrace{\tau_{yb}}^{5} + \overbrace{gD\frac{\partial \eta}{\partial y} + \frac{gD}{\rho_0}\int_{-1}^{0}\int_{\sigma}^{0}\left(D\frac{\partial \rho'}{\partial y} - \frac{\partial D}{\partial y}\sigma'\frac{\partial \rho'}{\partial \sigma}\right)d\sigma' d\sigma}^{6} = 0, \quad (1)$$

$$\overbrace{\frac{\partial vD}{\partial t}}^{1} + \overbrace{\frac{\partial uvD}{\partial x} + \frac{\partial v^2 D}{\partial y} + \frac{\partial v\omega}{\partial \sigma} - F_y}^{2} + \overbrace{fuD}^{3}\ \overbrace{-\frac{\partial}{\partial \sigma}\left(\frac{K_M}{D}\frac{\partial v}{\partial \sigma}\right)}^{4} + \overbrace{gD\frac{\partial \eta}{\partial y} + \frac{gD^2}{\rho_0}\int_{\sigma}^{0}\left(D\frac{\partial \rho'}{\partial y} - \frac{\sigma'}{D}\frac{\partial D}{\partial y}\frac{\partial \rho'}{\partial \sigma'}\right)d\sigma'}^{5} = 0 \quad (2)$$

where (V_b, v) and (U_b, u) are the alongshore and across-shore (depth-average, depth-dependent) velocity components, respectively, $D = H + \eta$ is the water depth, H is the undisturbed water depth, η is the surface elevation, F_{by} and F_y are the corresponding horizontal viscosity terms, G_y is the dispersion term [*Blumberg and Mellor*, 1987], τ_{ys} and τ_{yb} are alongshore components of the surface and bottom stress, respectively, ω is a velocity normal to σ surfaces, and K_M is the vertical turbulent viscosity coefficient.

[22] The numerical model equations are written in horizontal curvilinear coordinates. For simplicity in notation, we write the equations here in locally Cartesian form, but the variables are evaluated with respect to the curvilinear coordinates. In addition, before evaluation of terms in (1) and (2), we divide by H so that, assuming D is approximately equal to H, (1) corresponds to the depth-averaged momentum equation and the terms in (1) and (2) likewise have units ms^{-2}. The terms in (1) (divided by H) are referred to as (1) acceleration (ace), (2) nonlinear advection

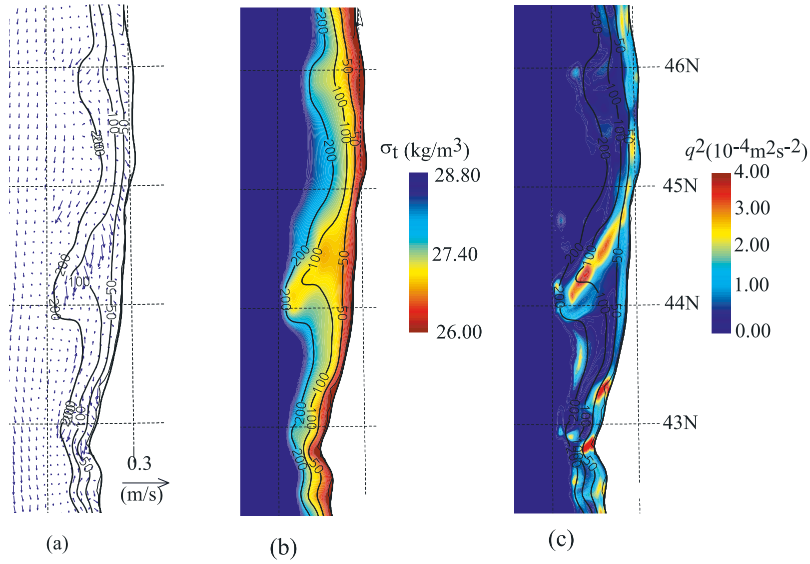

Figure 9. (a) Time mean bottom velocity vectors (m s^{-1}), (b) bottom σ_t (kg/m^3), and (c) time mean values of twice the turbulent kinetic energy (10^{-4} m^2 s^{-2}) at the bottom.

(adv), (3) Coriolis force (fU), (4) wind stress, (5) bottom stress, and (6) pressure gradient (P_y). In (2) (divided by H), terms 1 and 2 have the same designation, while 3 is the Coriolis force (fu), 4 is vertical diffusion (diff), and 5 is the pressure gradient p_y.

[23] For subinertial frequency shelf flows off Oregon the across-shore x momentum equation is dominated by geostrophic balance of the alongshore current v. Over variable shelf topography, the local "alongshore" direction, defined for example as aligned with the time mean depth-averaged velocity, typically does not coincide exactly with the curvilinear coordinate y. In that case, geostrophic balance from the local "alongshore velocity" tends to dominate the balances in both the x and the y momentum equations. Because of that fact, it is convenient to add the Coriolis force term 3 fU (or fu) and the pressure gradient term 6 P_y (or 5 p_y) and to consider the behavior of the sum, which is referred to here as the ageostrophic pressure gradient term, apg = $fU + P_y$ or apg = $fu + p_y$.

[24] In order to help ascertain when apg from (1) is dominated by pressure gradient forces it is useful to calculate the net contributions of fU and of P_y to apg. To do this, we follow the procedure used by *Gan and Allen* [2002b], and here in Section 6.2, to examine net contributions of x and y direction advection in the depth-averaged temperature equation. That procedure is described in Appendix A. The method of calculation of the net effects of the Coriolis force fU and of the pressure gradient P_y to apg from (1) is described in Appendix B.

5.1. Depth-Averaged Momentum Balances

[25] Fields of time mean values of terms in (1) together with the corresponding time mean values of the depth-averaged velocity vectors are plotted in Figure 11. Southward mean currents are forced by the southward mean wind stress, which in (1) is positive. The positive wind stress is generally retarded by a negative bottom stress. The offshore deflection of the coastal jet over Heceta Bank is clearly shown by the depth-averaged velocity vectors which also give a useful impression of the weakened depth-average circulation inshore of the jet over and south of the bank. The restrengthening, starting at about 44.2°N, of a southward current next to the coast, inshore of the offshore deflected coastal jet and inshore of the region of weakened circulation, is also evident.

[26] The large negative nonlinear advection term adv in regions near the coast from 44.7°N to 46°N and from 42.8°N to 43.8°N evidently reflects the spatial increase in magnitude southward of the southward coastal jet as the currents respond to narrowing shelf topography in the region between 46°N and 45°N or to the convergence of the reattaching offshore coastal jet with the near shore jet around 43.2°N. Indications of the spatial acceleration of the southward mean flow near 45°N also may be seen from the sections of v at lines 193 and 200 in Figure 10. Over Heceta Bank (43.8°N to 44.8°N), the nonlinear advection term adv is positive on the inshore side of the coastal jet, corresponding to the offshore deflection of the jet, and is balanced by a negative apg and by negative bottom stress. The region of negative bottom stress over the bank is consistent with the fields of bottom velocity and q^2 in Figure 9. Positive apg is found near the coast balancing adv in the regions mentioned above where adv is relatively large and negative. The plot of pre, the net contribution of the pressure gradient P_y to apg (Appendix B), shows that a positive pressure gradient typically contributes to the positive apg in those regions. Inshore of the 50 m isobath, the wind stress and the bottom stress are relatively large magnitude. Offshore of 50 m, however, the dominance of the terms adv, apg, and, to a lesser extent, bottom stress, reflects a more complex nonlinear response of the wind-forced flow to shelf topography.

[27] An additional point of interest is provided by the regions of (relatively weak) positive mean bottom stress over and south of Heceta Bank (43.3°N to 44.6°N), south of Cape Blanco (42.6°N to 42.8°N) and offshore between 45°N and 46°N. These correspond to regions of northward mean bottom currents in Figure 9 and represent a notable

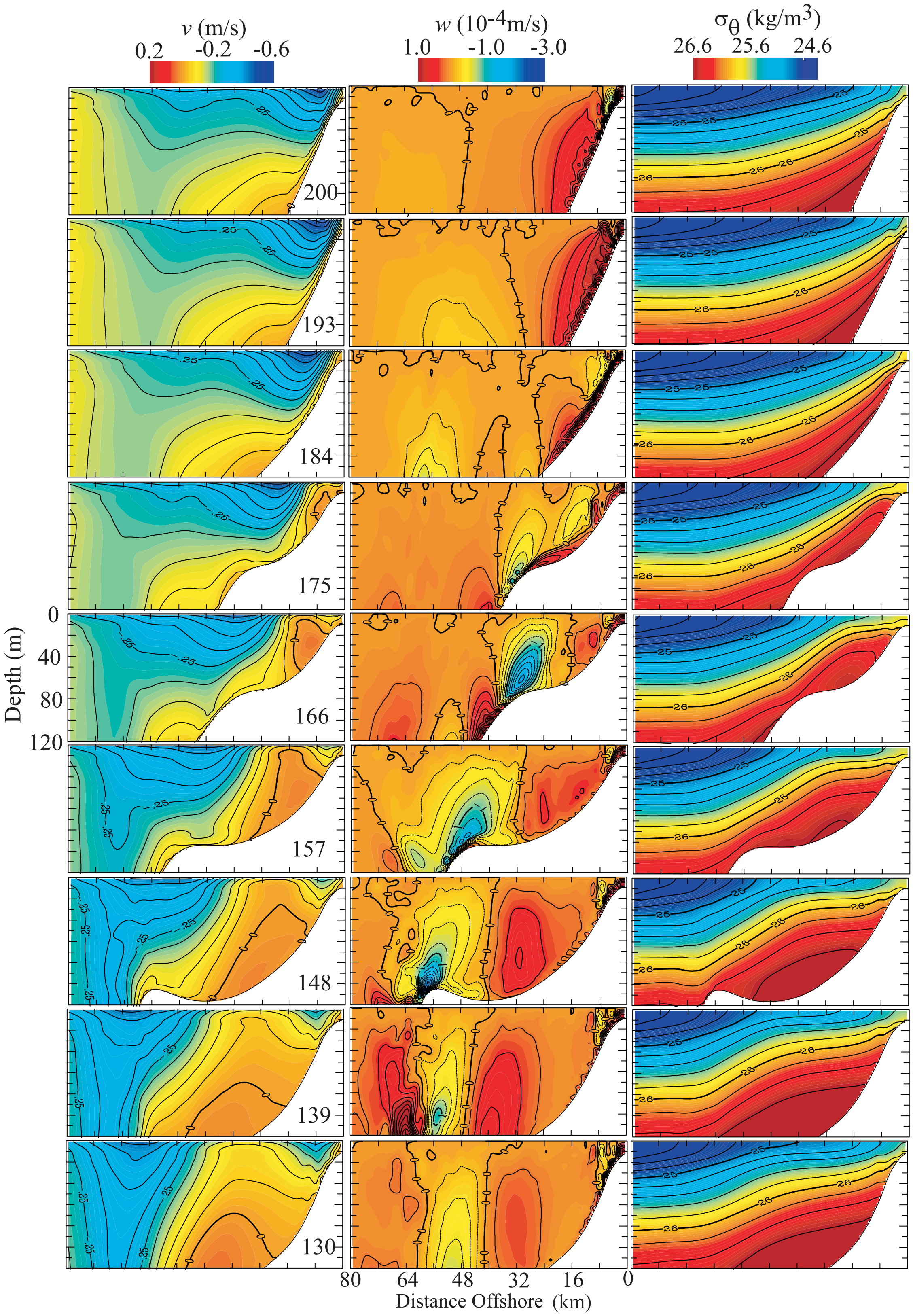

Figure 10. Across-shore sections of time mean values of alongshore velocity v (m s^{-1}), vertical velocity w (10^{-4} m s^{-1}), and potential density σ_θ (kg m^{-3}) from lines 200 to 130 shown in Figure 1. The thick contour lines are 0 m s^{-1} for v, 0 and -1 (10^{-4} m s^{-1}) for w, and 25 and 26 (kg m^{-3}) for σ_θ.

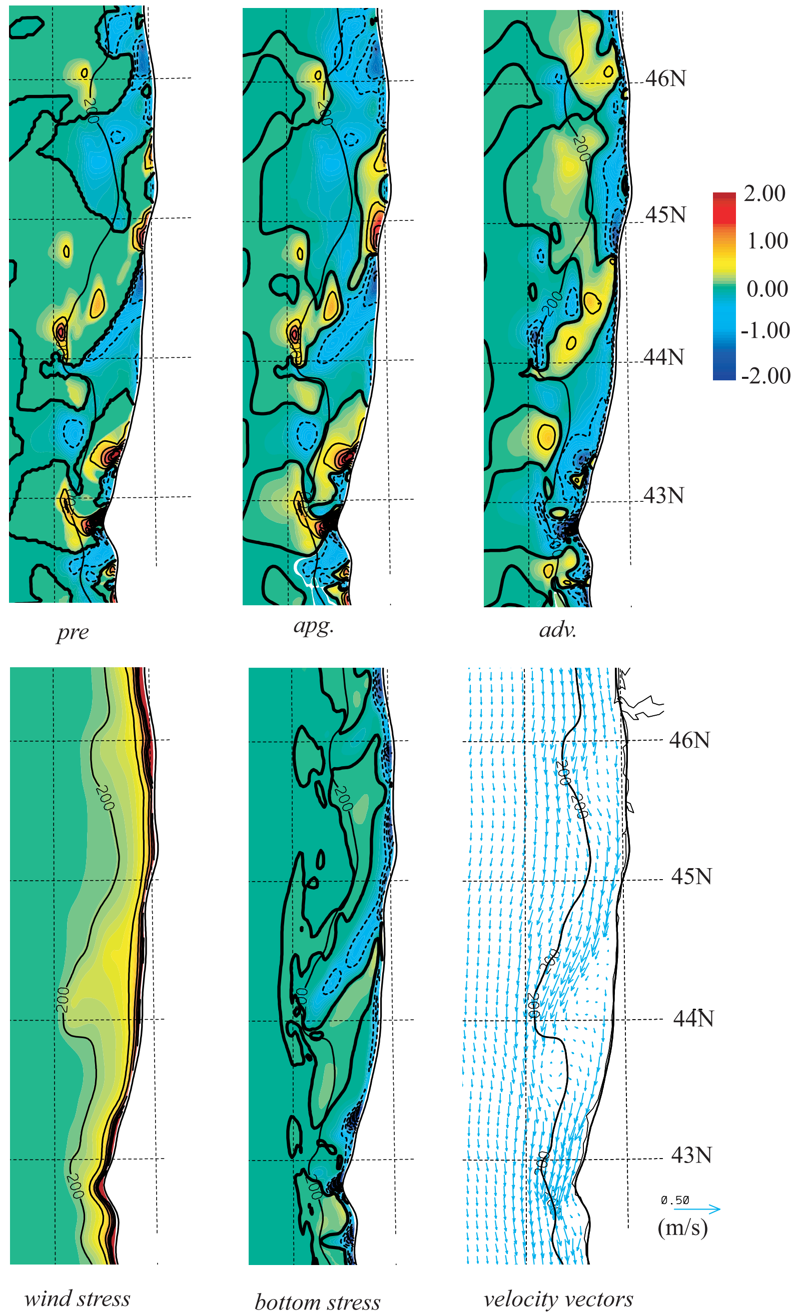

Figure 11. Time mean fields of terms from the depth-averaged alongshore momentum equation. Abbreviations are as follows: pre, net pressure gradient (Appendix B); apg, ageostrophic pressure gradient; adv, nonlinear advection; wind stress and bottom stress are divided by water depth and multiplied by 10^6 m s^{-2}. The corresponding time mean depth-averaged velocity vectors (m s^{-1}) are also plotted.

aspect of the shelf flow response to topography. As discussed in Section 4 in connection with Figure 9, on the south central part of Heceta Bank these near-bottom currents evidently advect dense water northward over the bank. The term balances in Figure 11 show that the positive bottom stresses over Heceta Bank and south of Cape Blanco are balanced primarily by a negative apg. The plot of pre shows that in these regions of northward bottom currents and negative apg, the dominant contribution to apg is from a negative, or northward, pressure gradient.

[28] To further investigate the dynamical response of the flow field forced by time-dependent wind stress and influenced by the bottom topography over the bank, the temporal and alongshore spatial variability of terms in (1) at a location approximately 8.5 km from the coast in the region around Heceta Bank is shown in Figure 12. The major features are summarized as follows: In response to southward wind stress events, a negative apg is formed south of Newport over the bank and is mainly balanced by a positive nonlinear advection term adv. This distinct spatial dynamical feature over the bank is strongly time-dependent.

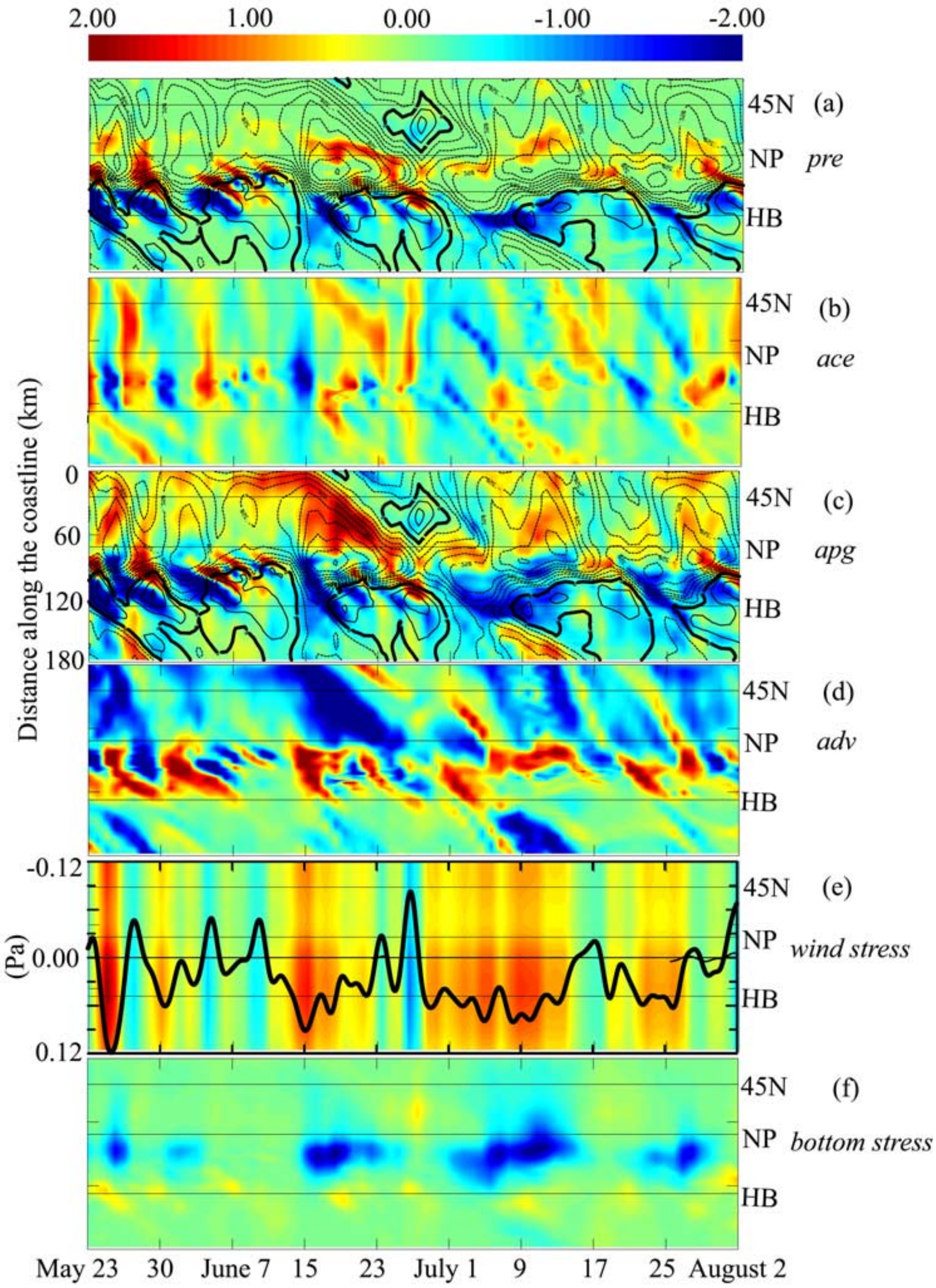

Figure 12. Depth average of (a) net pressure gradient (pre) (Appendix B), (b) acceleration (ace), (c) ageostrophic pressure gradient (apg), (d) nonlinear advection (adv), (e) wind stress, and (f) bottom stress terms (m s^{-2}, averaged over 24 hours, multiplied by 10^{6}) as a function of time and distance along the coast at locations approximately 8.5 km offshore from 43.8°N to 45.2°N. The locations of the lines 148 at Heceta Bank (HB), 175 at Newport (NP), and 200 at 45°N are marked. The contour lines in Figures 12a and 12c are alongshore velocity (m s^{-1}) with solid lines for northward and dashed lines for southward velocities, respectively. Time series of wind stress with a bold line for the north-south component is also shown in Figure 12e.

Southward wind stress events strengthen the southward coastal jet along the coast north of the bank. The positive adv corresponds to a spatial deceleration over the bank of this strengthened alongshore current. Northward currents, shown by solid contours in Figure 12, typically occur after a negative apg is set up and after the southward wind stress decreases in magnitude. The acceleration term ace south of Newport, which is negative during the southward wind events, correspondingly switches to positive values in response to the negative apg after the southward wind stress decreases. In Figure 12 the plot of pre, the net contribution of the pressure gradient P_y to apg (Appendix B), clearly shows that the negative apg values found south of Newport are primarily the result of negative values of P_y, which

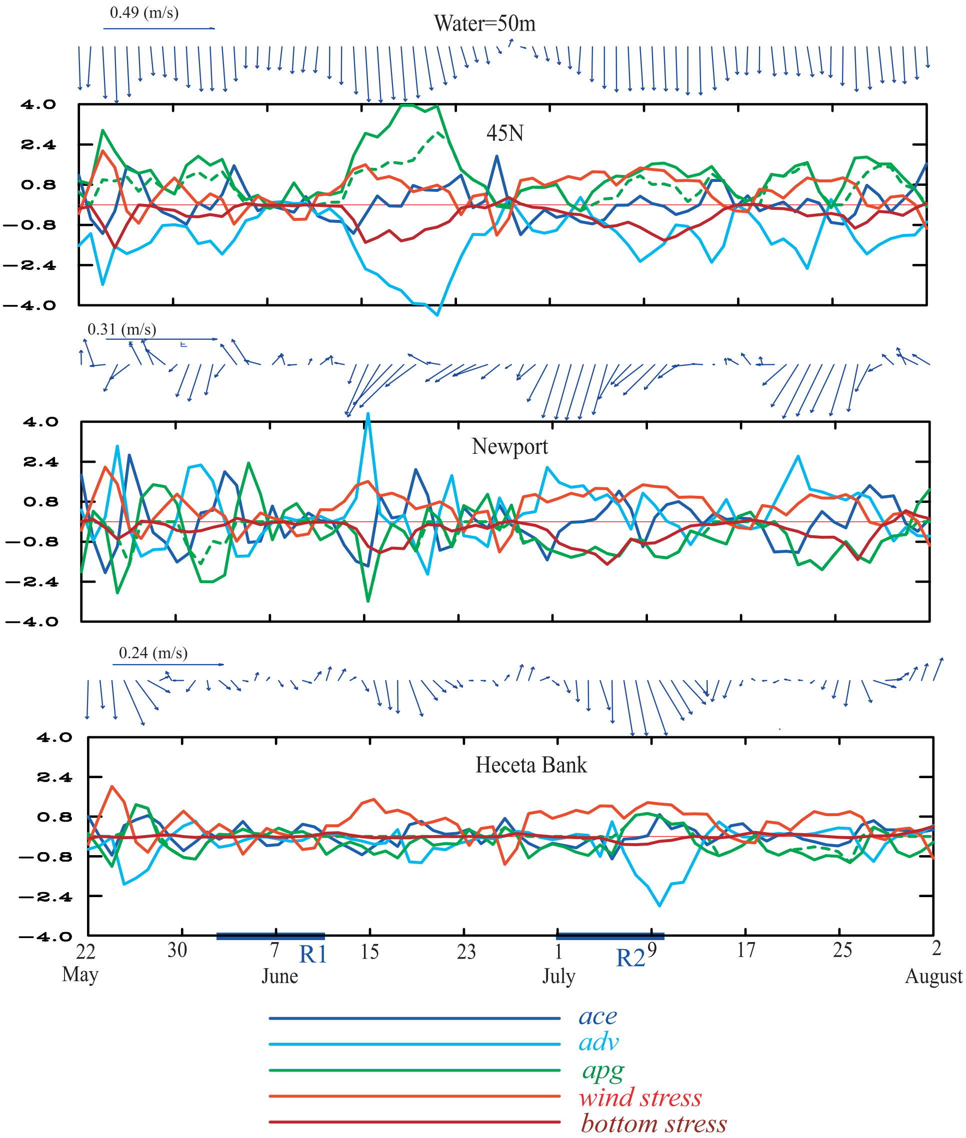

Figure 13. Time series of terms in the depth-averaged alongshore momentum equation (m s^{-2}, averaged over 24 hours, multiplied by 10^6) at water depths of 50 m along the 45°N northern mooring line (200), Newport line (175), and the southern mooring line (148). The dashed lines show the net contribution Cor from the Coriolis force to apg (Appendix B). Time series of corresponding daily averaged depth-averaged velocity vectors (m s^{-1}) from the same locations are also shown. The velocity vectors are plotted such that the vertical axis in the figure is aligned with the local y coordinate direction.

represent a northward pressure gradient force. North of Newport, the southward coastal jet accelerates spatially from 45°N to the region near Newport during southward winds as indicated by the alongshore velocity contours. This contributes to a negative value of nonlinear advection adv which is balanced by positive values of apg. Positive values of ace north of Newport are primarily a response to northward wind events, i.e., to a negative wind stress term. Figure 12 also shows that relatively large negative bottom stress values are found near Newport during strong positively (southward) wind stress, coincident with the presence of a relatively large southward jet. Strong negative bottom stress appears 2–3 days after the occurrence of positive wind stress reflecting the response time of the bottom alongshore currents at that location to the wind stress forcing.

[29] Time series of daily-averaged terms from (1) together with the corresponding depth-averaged velocity vectors from locations at 50 m and 100 m water depths near 45°N (line 200), Newport (line 175), and Heceta Bank (line 148) are shown in Figures 13 and 14 to illustrate their different dynamical balances in response to the controls of different shelf bottom topography. In 50 m water depth at 45°N, north of the bank, a positive ageostrophic pressure gradient apg and negative nonlinear advection adv are generally the largest magnitude terms and they tend to

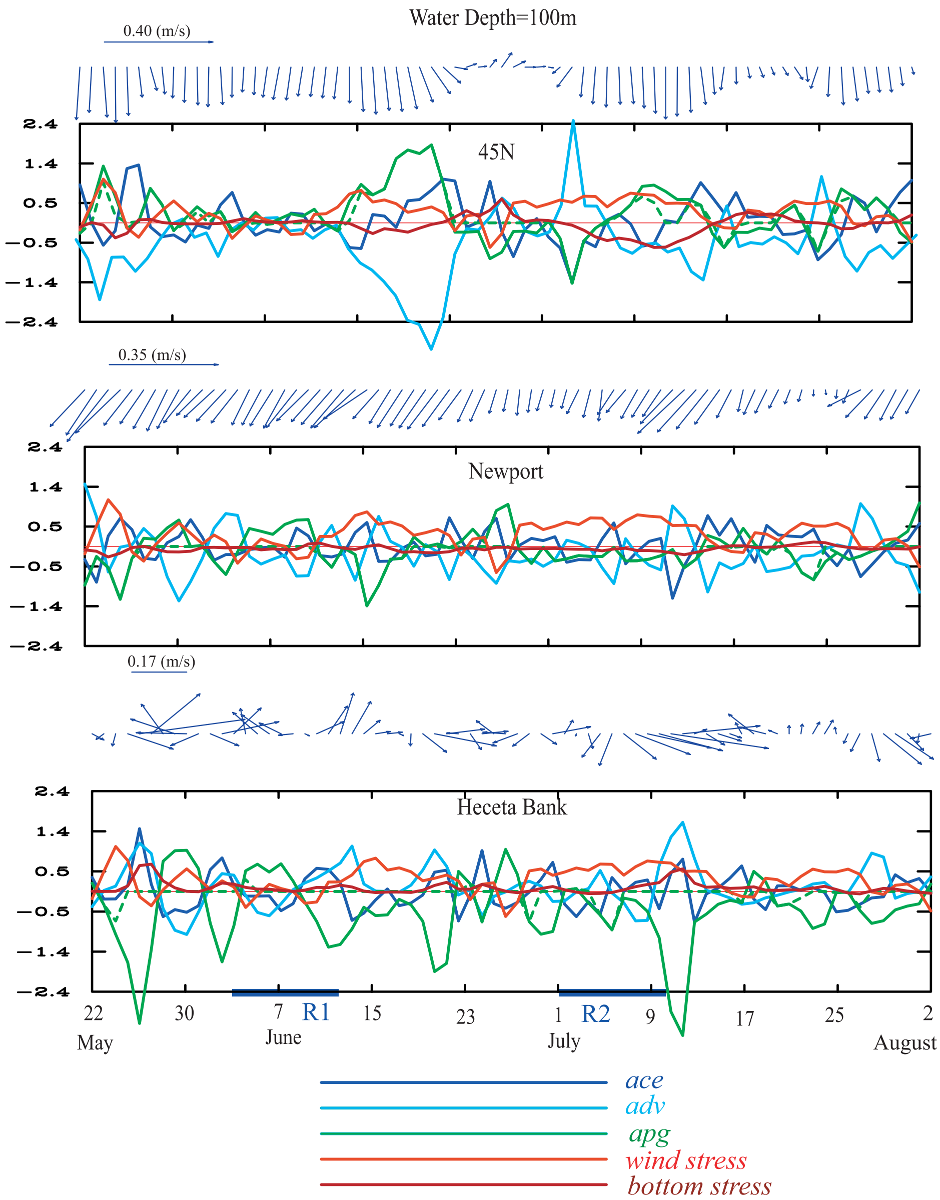

Figure 14. Same as Figure 13, but at water depths of 100 m. The scale for the magnitude in these plots is smaller than that in Figure 13 at water depths of 50 m.

balance each other. Their magnitudes increase 2–3 days after southward upwelling favorable winds intensify. The negative adv values result from the spatial acceleration southward of the coastal jet in this region as noted before. In Figure 13, a plot of Cor, the net contribution of the Coriolis force to apg (Appendix B), shows that the positive apg values are the result of positive values of both the Coriolis force fU and the pressure gradient P_y. Wind stress is initially balanced by the acceleration term and subsequently by bottom stress 1–2 days later. The coastal currents are directed southward generally parallel to the coastline. In 50 m water depth off Newport, the southwestward direction of the currents reflects the offshore veering of the coastal jet by the bank. During the southwestward flow events, adv is positive corresponding to the southward spatial deceleration of the southward currents over the bank and is balanced by a negative apg that is mainly related to negative values of Cor. The magnitudes of the ageostrophic pressure apg and nonlinear advection adv terms at this location are smaller, relative to the other terms, than they are at 45°N. Bottom stress magnitudes are appreciable here, as they are at 45°N, in balancing the wind stress. At 50 m water depth in the south at Heceta Bank, different conditions are found. The currents fluctuate in response to the wind stress similar to 45°N, but with more occurrences of northward flow. In general, positive values of wind stress are the dominant term which balances the rest of terms which have negative values. Although apg is negative most of time, it turns positive when southward winds increase in order to balance a negative nonlinear advection term adv that represents the southward spatial increase of the southward currents near the coast as noted before in connection with Figure 11.

[30] At the offshore locations of 100 m water depth (Figure 14), the response at 45°N is qualitatively similar

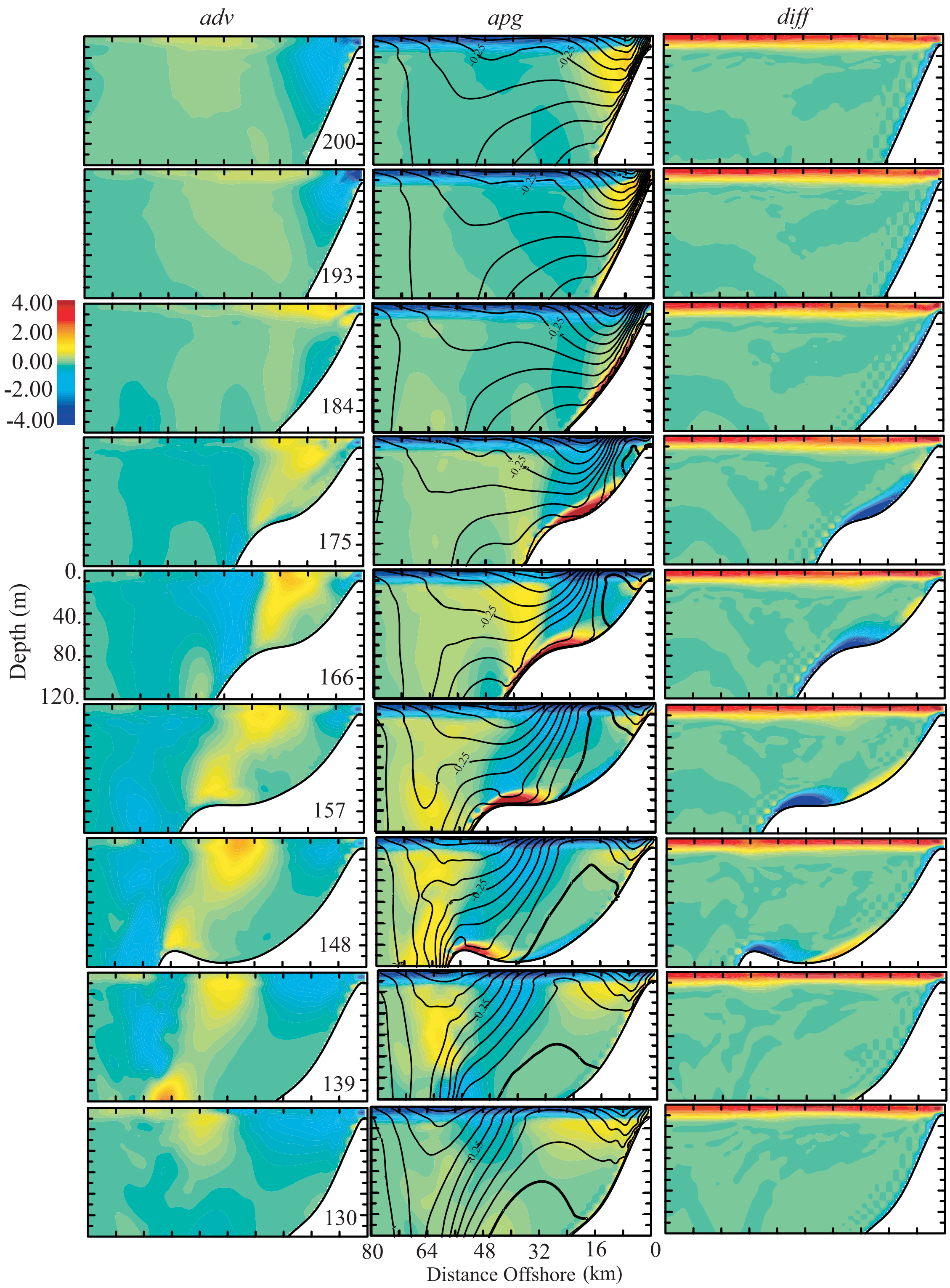

Figure 15. Across-shore sections of time mean values of nonlinear advection (adv), ageostrophic pressure gradient (apg), and vertical diffusion (diff) terms in the alongshore momentum equation (2) divided by the water depth at lines from 45°N to south of Heceta Bank (in m s^{-2}, multiplied by 10^6). The alongshore velocity v is also superimposed on the fields of apg.

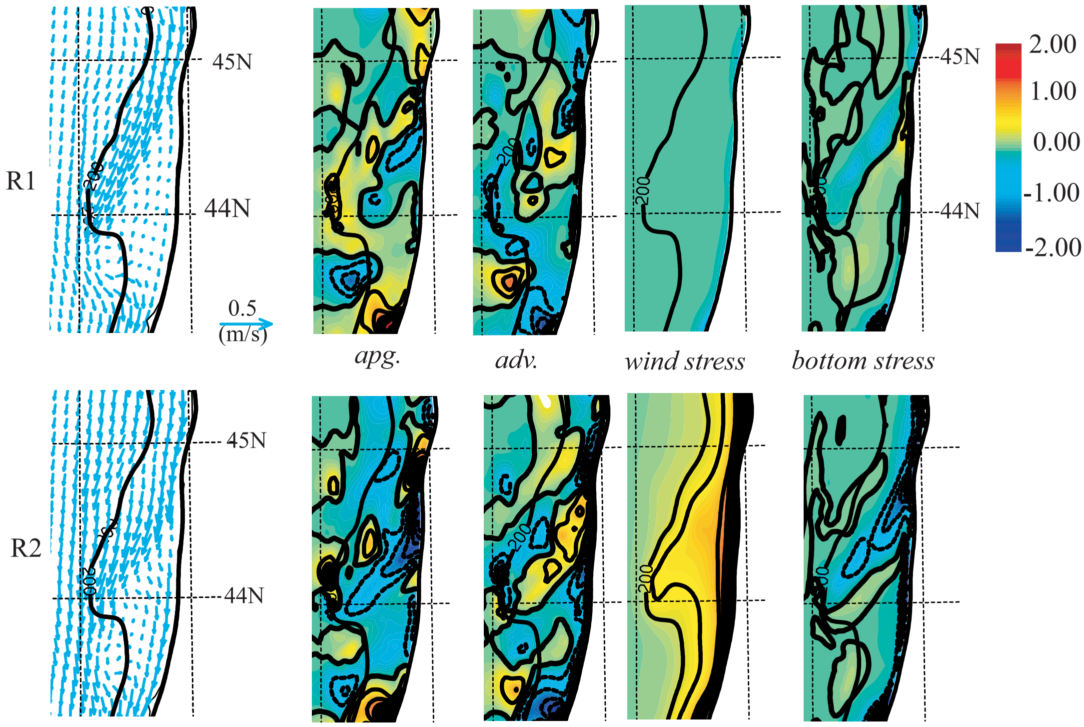

Figure 16. Fields of time mean depth-averaged velocity vectors (m s^{-1}) and time mean fields of term from the depth-averaged alongshore momentum equation: apg, ageostrophic pressure gradient; adv, nonlinear advection; wind stress; and bottom stress (divided by water depth and multiplied by 10^6 m s^{-2}). The time averaged periods are 3–12 June for regime 1 (R1), dominated by northward wind forcing, and 1–10 July for regime 2 (R2), dominated by southward wind forcing.

to that at the nearshore station in 50 m water depth, except that the bottom stress is relatively smaller in magnitude. Also, there are brief periods around 2 July and 25 July where adv shows positive spikes, possibly reflecting eddy-like fluctuations in the coastal jet. Off Newport at 100 m water depth, the bottom stress term is very small. A different characteristic of the balances here is the occurrence of events of apparent direct response of the acceleration term ace to fluctuations in adv, including a positive response on 30 May and 22 June and a negative response on 10 and 27 July. The behavior of the terms at Heceta Bank in 100 m water depth is different from those there in 50 m water depth. Dominant behavior involves large negative fluctuations in apg which balance both positive adv and a positive acceleration ace corresponding to either a deceleration of southward currents, e.g., on 20 June and 11 July, or an acceleration of northward currents, e.g., on 23 May and 2 June. The behavior of Cor at Heceta Bank 100 m water depth, characterized by mostly zero values, clearly indicates that the negative values of apg that accelerate the currents northward are due primarily to negative values of the pressure gradient P_y, corresponding to a northward pressure gradient force, consistent with the results indicated by pre in Figure 12. In general, the magnitudes of terms in the alongshore momentum equations are relatively small at 100 m compared to those at 50 m water depths.

[31] Overall, the term balances in Figures 11–14 demonstrate complex time- and space-dependent dynamics in the coastal flow adjustment to the topography of Heceta Bank. Additional information may be obtained from depth-dependent alongshore momentum balances which are examined next.

5.2. Depth-Dependent Momentum Balances

[32] The alongshore variation of the time-mean depth-dependent dynamical balances of the shelf flow can be analyzed from term balances of (2) at different across-shore sections along the same lines as in Figure 10, running from north (45°N) to south (42.2°N). The time mean values of the nonlinear advection adv, ageostrophic pressure gradient apg, and vertical diffusion diff terms from (2) at these sections are shown in Figure 15 with the mean alongshore velocity v from Figure 10 superimposed on apg. Positive values of diff near the surface reflect the response in a turbulent boundary layer of about 15 m depth to the mean upwelling favorable wind stress. Similarly, relatively large magnitude values of diff are found in boundary layers at the bottom. North of line 184, in the region with relatively small alongshore variations in bottom topography, a bottom frictional layer with negative values of diff extends from the midshelf to the coast. Relatively large vertical (Figure 10) and onshore (not shown) velocities in this near-bottom region correspond to onshore upwelling transport in a bottom Ekman layer. South of section 184 in the region around Heceta Bank, the negative diff bottom layer shifts seaward due to the offshore veering of the coastal jet. From sections 175 to 148, positive values of diff are found in bottom layers under the northward currents on the shoreward side of the jet.

[33] The vertical and across-shelf scales of adv and age are closely related to the corresponding structure of the

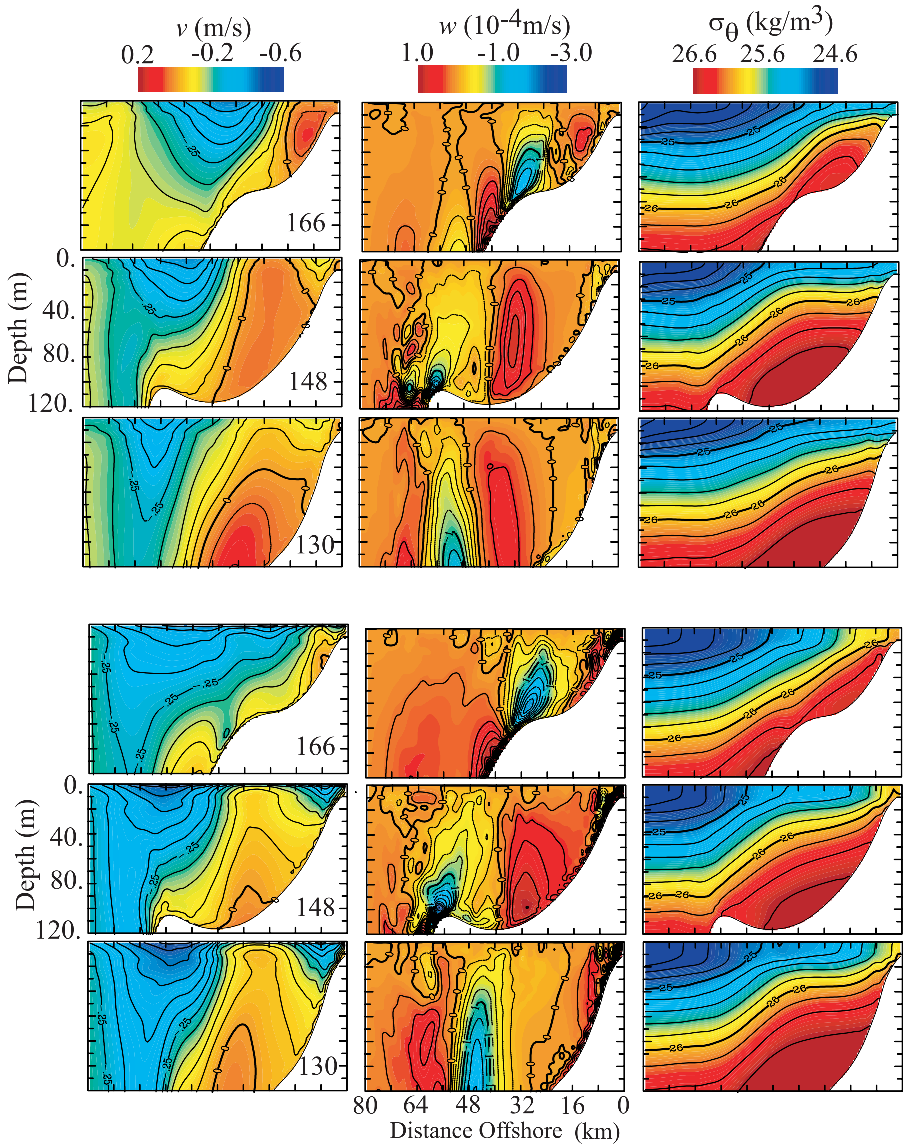

Figure 17. Across-shore sections of time mean values of alongshore velocity (m s^{-1}), vertical velocity (10^{-4} m s^{-1}), and potential density (kg m^{-3}) at lines 166, 148, and 130 shown in Figure 1 for regimes dominated by (top) northward winds (R1) and by (bottom) southward winds (R2). The bold contour lines are 0 m s^{-1} for v, 0 and -1 (10^{-4} m s^{-1}) for w, and 25 and 26 (kg m^{-3}) for σ_θ.

mean alongshore velocity in the jet. The influence of the variable shelf topography on the dynamical balances is shown by the existence of opposite signs of adv on the inshore side of the jet north and south of line 184. North of 184, a positive apg is balanced by a negative adv which is evidently caused by spatial acceleration of the alongshore current as discussed before in connection with Figures 10, 11, and 13. As the jet moves south of line 175, the offshore veering and accompanying spatial deceleration of the southward mean alongshore current over the bank result in a positive nonlinear advection adv on the shoreward side of the jet balanced by a negative apg. Between lines 166 and 139, relatively large negative adv and corresponding positive apg are found on the seaward side of the jet, reflecting the offshore advection of the southward jet. From line 166 south, the increase in strength of a southward coastal jet redeveloping next to the coast is reflected by growing regions of negative values of adv which have structure at line 139 qualitatively similar to that found north at line 200.

6. Flow Features During Time Periods With Differing Wind Conditions

6.1. Dynamical Balances

[34] To help clarify the relationship of the time-dependent wind forcing to the shelf flow response over the bank, conditions are examined for two different 10 day periods dominated, respectively, by weak fluctuating northward winds, 3–12 June, regime R1, and by sustained southward winds, 1–10 July, regime R2 (Figure 2). The corresponding ecosystem response during these same time periods is investigated by *Spitz et al.* [2005] where a marked qualitative difference in behavior of the spatially average phytoplankton concentrations over the shelf, decreasing during

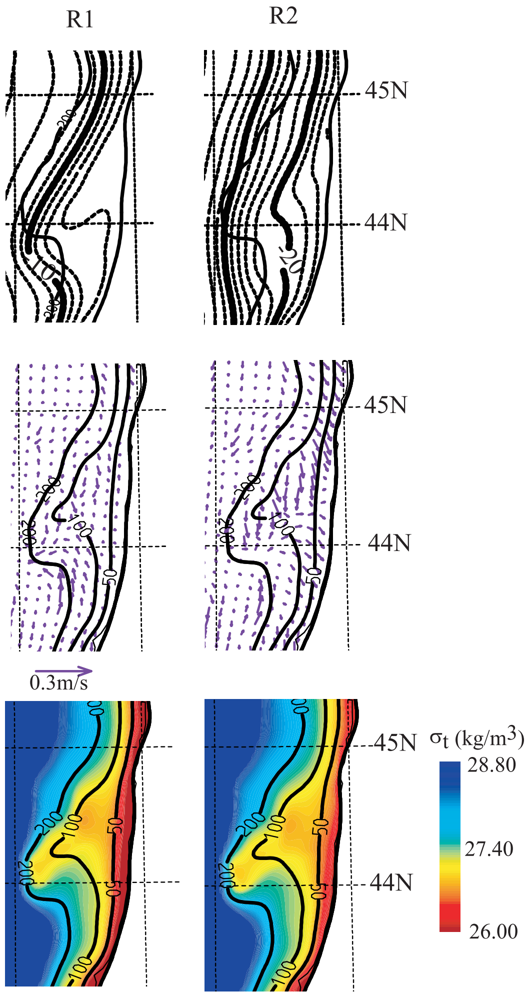

Figure 18. Fields of time mean surface elevation (cm), bottom velocity (m s^{-1}), and bottom σ_t (kg m^{-3}) for periods of R1 and R2, respectively.

R1 and increasing during R2, is found. The time-averaged depth-averaged velocity vectors, along with time-averaged fields of terms in (1) for both time periods are shown in Figure 16. The alongshore coastal jet is clearly visible in both regimes. During R1, the jet is deflected farther offshore over the bank. Northward depth-averaged currents are found near the coast inshore of the jet indicating the presence of a cyclonic circulation over the bank from about 44.3°N to 44.7°N. The wind stress is weakly negative during R1 and the region of negative bottom stress is reduced in magnitude and displaced offshore compared to R2, corresponding to the offshore displacement of the coastal jet. An extensive region of positive bottom stress, corresponding to northward bottom currents is found inshore of the coastal jet from 43.5°N to 44.8°N during R1. From 44°N to 44.8°N that positive bottom stress is balanced primarily by a negative apg. During R2, the relatively large positive southward wind stress is evident, as is the corresponding large negative bottom stress under the coastal jet. The general structure of the adv and apg fields during R2 is similar to that found in the 72 day time mean fields in Figure 11, but with generally larger magnitudes. During R1 the structures of adv and apg remain qualitatively similar to those during R2, but with much smaller magnitudes.

[35] Alongshore velocity v, vertical velocity w, and potential density sections at lines 130, 148, and 166, spanning the south part of the bank are shown in Figure 17 for R1 and R2. Although the fields in Figure 17 are qualitatively similar in the two regimes, stronger northward currents ($v > 0$), generally greater upward motion ($w > 0$) at middepth, and an associated upward extension of the high-density water pool over the midshelf are found over the bank on line 148 during R1. Since the mean wind magnitude is very small in R1, the circulation during that period reflects the adjustment of the previously wind-forced flow to the variable shelf topography.

[36] Time mean fields of surface elevation, bottom velocity vectors, and bottom density during R1 and R2 are shown in Figure 18. The surface elevation field indicates the existence of both negative $\partial\eta/\partial y$ and positive $\partial\eta/\partial x$ on the shoreward side of jet over the bank during R1. These pressure gradients presumably partially reflect geostrophic balance of onshore and northward currents, respectively (Figures 16 and 19). The surface elevation field also gives a good indication, for the part of the pressure gradients that are not geostrophically balanced, how a northward pressure gradient force is set up over the bank during R1. Strong positive vertical velocities w and positive northward currents v are found over the bank on lines 148 and 166 during R1 (Figure 17). The large positive w in R1, however, does not lead to an increase of surface density. Instead, together with the northward alongshore currents v, it upwells the denser water from south of the bank and forms a pool of a high-density water over the midshelf. The existence of that feature of the circulation is also shown by the northward bottom velocity vectors and by the relatively larger values of the bottom density in the south and central parts of the bank during R1 (Figure 18). During R2, the nearly alongshore uniform surface elevation field, with increased across-shore gradients, reflects the strengthened alongshore coastal jet. The bottom velocity vectors show relatively strong onshore flow in boundary layers under the coastal jet. The bottom density field during R2 shows generally larger values on the shelf, especially inshore of the 50 m isobath, except offshore under the coastal jet at the southern tip of Heceta Bank where less dense water is evidently advected offshore under the intensified coastal jet.

6.2. Thermal Balances

[37] The time mean surface velocity and surface temperature fields over the bank during R1 and R2 are shown in Figure 19. Colder water is found at the surface near the coast during R2, consistent with the surfaced isopycnals in the density sections in Figure 17 and reflecting the results of upwelling processes during this period. In order to examine the relative contributions from across-shore and alongshore advection to changes in the temperature field during R1 and R2, terms in the time- and depth-averaged potential temperature equation have been calculated as by *Gan and Allen* [2002b] and plotted in Figure 19. The procedure is described in Appendix A. The advection terms, written in conservation form in POM, are rewritten to remove the contribution of the continuity equation. In addition, only the net contributions of across-shore ADVX and alongshore

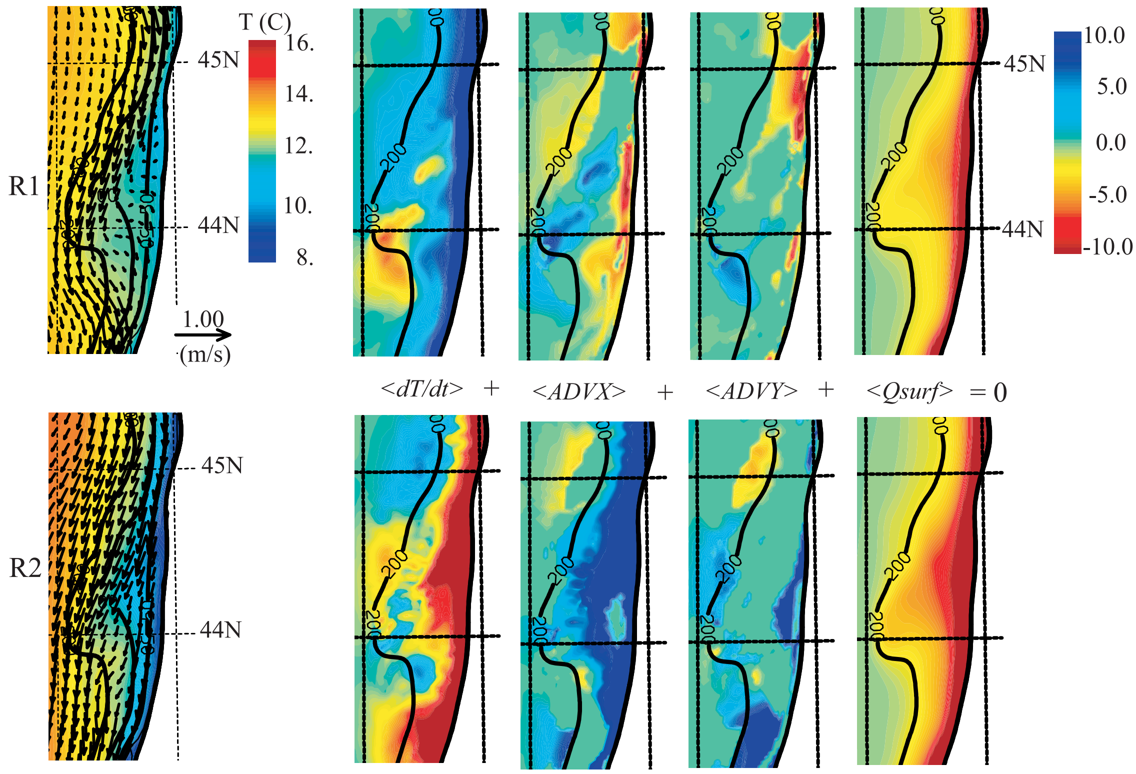

Figure 19. Fields of time mean surface velocity vectors (m s^{-1}), surface temperature (°C), and time-averaged values of terms (Cs^{-1}, multiplied by 10^{-7}) in the depth-averaged temperature equation calculated as described in Appendix A: ⟨ADVY⟩ alongshore advection, ⟨ADVX⟩ across-shore advection, ⟨dT/dt⟩ time rate of temperature change and ⟨Q_{surf}⟩ surface heat flux. The time-averaged periods are 3–12 June for regime 1 (R1), dominated by northward wind forcing, and 1–10 July for regime 2 (R2), dominated by southward wind forcing.

ADVY advection to the temperature change dT/dt are plotted. Time averages are denoted by angle brackets.

[38] During R2, ⟨dT/dt⟩ is strongly negative inshore of the 100 m isobath, reflecting net cooling, and is balanced primarily by positive across-shore advection ⟨ADVX⟩, although alongshore advection ⟨ADVY⟩ is also positive and contributes to the balance between 44°N and 44.8°N and south of 43.5°N. These positive advection terms also balance the negative surface heat flux ⟨Q⟩, which, compared to R1, has increased magnitudes near the coast where cold upwelled surface water leads to larger air-sea temperature differences.

[39] During R1, ⟨dT/dt⟩ is generally positive with larger magnitudes inshore of the 50 m isobath. In these regions there is net warming which is primarily caused by surface heat flux with contributions nearshore from across-shore advection ⟨ADVX⟩ between 43.8°N and 44.6°N and from alongshore advection ⟨ADVY⟩ between 44.6°N and 45.2°N. Over the bank, ⟨ADVX⟩ is positive and contributes to cooling. In the southern part of the bank there is a region of negative ⟨dT/dt⟩ showing net cooling. The negative ⟨dT/dt⟩ values at the southwest edge of the bank are balanced by positive values of both ⟨ADVY⟩ and ⟨ADVX⟩ that evidently reflect the advective effect of the northward and shoreward currents that intensify in that region during R1 (Figures 16 and 18).

[40] Time series of daily-averaged terms in the depth-averaged temperature equation (Appendix A) from locations 8 km offshore at 45°N (line 200), Newport (line 175), and Heceta Bank (line 148) (Figure 20) show the time-dependent contributions to dT/dt from ADVX, ADVY and surface heat flux Q in response to fluctuations in the wind stress. At 45°N and at Newport, the balances clearly show that cooling associated with upwelling winds (negative dT/dt) is contributed primarily by across-shore advection ADVX.

[41] Warming at 45°N, associated with northward winds and with the relaxation of southward winds, on the other hand, is contributed primarily by alongshore advection ADVY. At Newport, the warming events on 5 June and 19 July, following short periods of weak northward winds, are due to across-shore advection ADVX, while the warming event on 25 June is caused by alongshore advection ADVY. In contrast, at the Heceta Bank location, the cooling responses related to upwelling winds are contributed primarily by alongshore advection ADVY, while warming events are caused by ADVX.

7. Summary

[42] A high-resolution three-dimensional coastal ocean model has been used to simulate the upwelling circulation over the continental shelf off the Oregon coast during the COAST field experiment in summer 2001. On the basis of comparisons with data, the model, forced with observed time-varying wind stress and heat flux, does a reasonably good job of simulating observed conditions over the shelf.

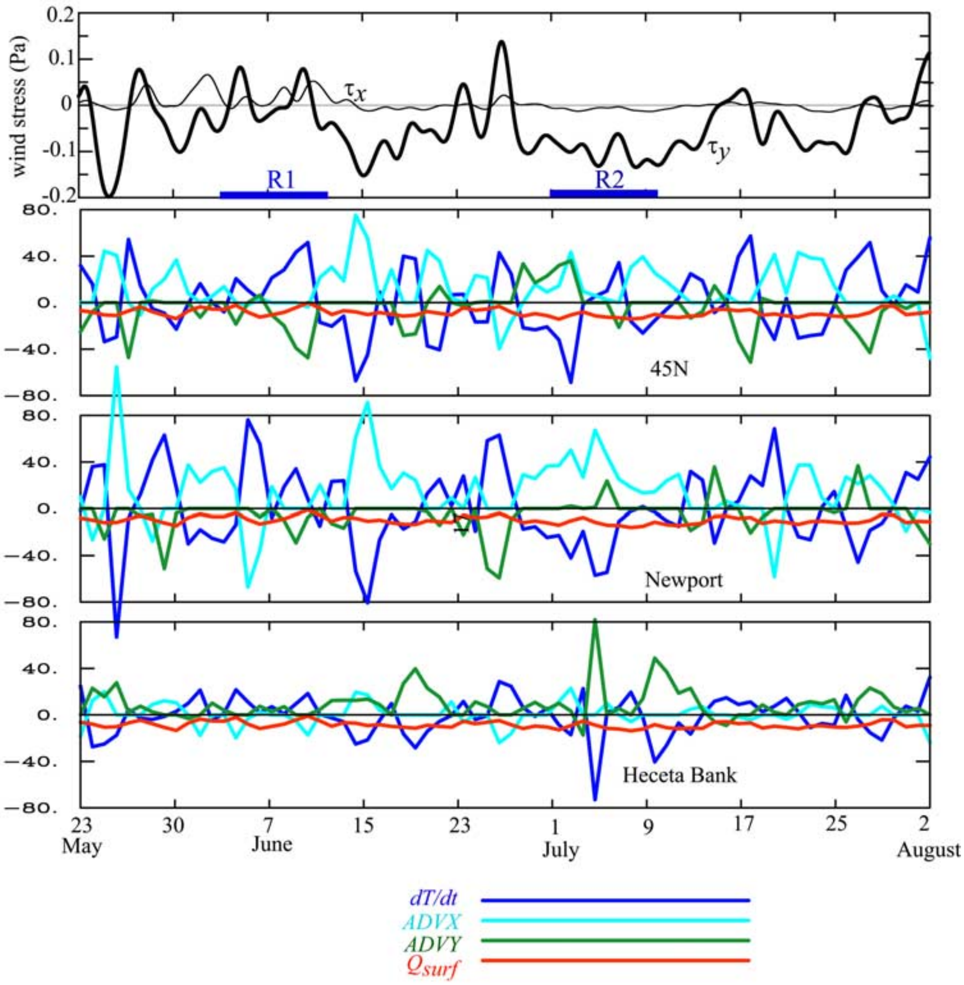

Figure 20. Time series of terms in the depth-averaged temperature equation (Cs^{-1}, multiplied by 10^{-7}) calculated as described in Appendix A at about 8 km offshore at 45°N (line 200, water depth 64 m), Newport (line 175, water depth 58 m), and Heceta Bank (line 148, water depth 63 m). The corresponding time series of wind stress near Newport is also shown.

The corresponding behavior in an embedded ecosystem model has been examined in the companion study by *Spitz et al.* [2005]. The model results shows that the flow field off the central Oregon coast is characterized by strong spatial and temporal variability resulting from the interaction of the wind-driven currents with the complex shelf topography associated with Heceta Bank. The objective of this study is to investigate the dynamical processes associated with this interaction through examination of the structure of the three-dimensional flow fields and through analyses of the alongshore momentum balances and the thermal balances.

[43] Documentation of the change in flow structure and identification of the dominant balances in the alongshore momentum equation as a function of across-shelf position and latitude between 43.8°N and 45°N has provided new information about the complex spatial and temporal variations in the dynamics of the shelf flow processes associated with Heceta Bank. Determination of the differences in the shelf flow response during two 10 day time periods with, respectively, dominantly northward and dominantly southward winds, has helped to clarify the dynamical origin of characteristic components of the mean and time-dependent circulation over the bank. An analysis of the behavior in the depth-integrated temperature equation during R1 and R2 likewise gives new information concerning the relative roles, as a function of location, of across-shore and alongshore advection on the net temperature changes during these periods.

[44] The mean southward alongshore upwelling jet is deflected offshore following the offshore excursion of the isobaths around Heceta Bank. This offshore deflection is accompanied by the presence of northward mean currents on the inshore side of the jet. Relatively cold surface waters are found near the coast and over Heceta Bank. The offshore deflection of the wind-forced jet is characterized, on the shoreward side of the jet, by a balance between positive nonlinear advection adv and negative ageostropic pressure gradient apg, which over the bank is primarily due to a negative pressure gradient P_y. When the southward upwelling winds relax, the negative pressure gradient accelerates currents on the inshore side of the jet northward. This process helps to establish a pattern in the mean circulation with northward currents found over the bank inshore of the offshore deflected jet. These northward mean currents

generally provide the mass flux for a second coastal jet that develops next to the coast and strengthens toward the south. The northward currents in addition advect relatively dense water onto the bank from the south and form a high-density pool of water over the midshelf. The thermal balances show that, in response to upwelling winds, cooling on the inner shelf over most of the region is caused primarily by across-shore advection, except on the inner shelf over Heceta Bank where alongshore advection also makes a significant contribution.

Appendix A: Potential Temperature Equation

[45] The depth-integrated equation for potential temperature is

$$\int_{-1}^{0} \frac{\partial \Theta D}{\partial t} d\sigma + \int_{-1}^{0} \frac{\partial \Theta u D}{\partial x} d\sigma + \int_{-1}^{0} \frac{\partial \Theta v D}{\partial y} d\sigma + \int_{-1}^{0} \frac{\partial \Theta \omega}{\partial \sigma} d\sigma - \int_{-1}^{0} \frac{\partial}{\partial \sigma}\left(\frac{K_H}{D}\frac{\partial \Theta}{\partial \sigma}\right) d\sigma - \int_{-1}^{0} F_{\Theta} d\sigma - \int_{-1}^{0} \frac{\partial R}{\partial \sigma} d\sigma = 0, \tag{A1}$$

where Θ is potential temperature, $D = H + \eta$ is the water depth, H is the undisturbed water depth, η is the surface elevation, K_H is the vertical diffusivity coefficient, F_{Θ} represents horizontal diffusion, R is short wave radiation flux, and the velocity components are defined in Sections 2 and 5. The nonlinear advection terms are written in conservation (or divergence) form:

$$\mathrm{DADV} = \int_{-1}^{0} \frac{\partial \Theta u D}{\partial x} d\sigma + \int_{-1}^{0} \frac{\partial \Theta v D}{\partial y} d\sigma + \int_{-1}^{0} \frac{\partial \Theta \omega}{\partial \sigma} d\sigma. \tag{A2}$$

[46] To evaluate the relative contribution of alongshore and across-shore temperature advection, it is necessary to remove terms in the continuity equation from (A2). Since, for daily time averages, the contribution of η_t in the continuity equation is relatively small, that balance is well approximated by

$$\frac{\partial u D}{\partial x} + \frac{\partial v D}{\partial y} + \frac{\partial \omega}{\partial \sigma} = 0. \tag{A3}$$

The depth-averaged form of (A3) is

$$\frac{\partial U_b D}{\partial x} + \frac{\partial V_b D}{\partial y} = 0. \tag{A4}$$

[47] We rewrite the individual advection terms in the form

$$\mathrm{DADVY} = \int_{-1}^{0} \left(\frac{\partial \Theta v D}{\partial y} - \Theta \frac{\partial V_b D}{\partial y} \right) d\sigma \tag{A5}$$

$$\mathrm{DADVX} = \int_{-1}^{0} \left(\frac{\partial \Theta u D}{\partial x} - \Theta \frac{\partial U_b D}{\partial x} \right) d\sigma_6. \tag{A6}$$

As a result of the boundary condition $\omega = 0$ at $\sigma = 0, -1$, the last term on the right-hand side of (A2) is zero so that with (A4),

$$\mathrm{DADV} = \mathrm{DADVY} + \mathrm{DADVX}. \tag{A7}$$

[48] In Figure 20 we plot time series of the terms in (A1) (converted to depth averages by dividing by H) at three locations. We start by defining

$$\mathrm{ADVY}_I = H^{-1}\mathrm{DADVY}, \tag{A8}$$

$$\mathrm{ADVX}_I = H^{-1}\mathrm{DADVX}, \tag{A9}$$

$$\frac{dT}{dt} = H^{-1} \int_{-1}^{0} \frac{\partial \Theta D}{\partial t} d\sigma, \tag{A10}$$

$$Q_{\mathrm{surf}} = -H^{-1}\left(\int_{-1}^{0} \frac{\partial}{\partial \sigma}\left(\frac{K_H}{D}\frac{\partial \Theta}{\partial \sigma}\right) d\sigma + \int_{-1}^{0} \frac{\partial R}{\partial \sigma} d\sigma \right), \tag{A11}$$

where DADVY and DADVX are given by (A5) and (A6), respectively, and where we assume H approximately equals D. To help identify the net contributions of ADVY_I and ADVX_I to dT/dt, we further remove any common part of opposite sign that cancels in their sum:

$$\mathrm{ADV} = \mathrm{ADVY}_I + \mathrm{ADVX}_I. \tag{A12}$$

For example, for ADV > 0, we define

$$\mathrm{ADVX} = \frac{1}{2}(\mathrm{ADVX}_I + |\mathrm{ADVX}_I|) + \frac{1}{2}(\mathrm{ADVY}_I - |\mathrm{ADVY}_I|) \tag{A13}$$

$$\mathrm{ADVY} = \frac{1}{2}(\mathrm{ADVY}_I + |\mathrm{ADVY}_I|) + \frac{1}{2}(\mathrm{ADVX}_I - |\mathrm{ADVX}_I|). \tag{A14}$$

As a result, the sum is preserved, i.e.,

$$\mathrm{ADV} = \mathrm{ADVY} + \mathrm{ADVX}, \tag{A15}$$

and the common part of opposite sign that would cancel in the sum is removed. For ADV < 0, (A13) and (A14) are altered by reversing the signs of the terms with absolute values.

[49] In Figure 19 we plot the spatial distributions of the terms time averaged over the respective 10 day time periods of R1 and R2. These are calculated in the following manner, where an angle bracket denotes a time average over the time interval $t_f = t_2 - t_1$:

$$\left\langle \frac{dT}{dt} \right\rangle = t_f^{-1} \int_{t_1}^{t_2} \frac{dT}{dt} dt, \tag{A16}$$

$$\langle Q_{\mathrm{surf}} \rangle = t_f^{-1} \int_{t_1}^{t_2} Q_{\mathrm{surf}} dt, \tag{A17}$$

$$\langle \mathrm{ADVX}_I \rangle = t_f^{-1} \int_{t_1}^{t_2} \mathrm{ADVX}_I dt, \tag{A18}$$

$$\langle \mathrm{ADVY}_I \rangle = t_f^{-1} \int_{t_1}^{t_2} \mathrm{ADVY}_I dt. \tag{A19}$$

[50] Following this computation, the common parts of $\langle \mathrm{ADVX}_I \rangle$ and $\langle \mathrm{ADVY}_I \rangle$ are removed using (A13) and (A14) to form $\langle \mathrm{ADVX} \rangle$ and $\langle \mathrm{ADVY} \rangle$, with the signs of the terms with absolute values determined according to the sign of $\langle \mathrm{ADV} \rangle$. Note that this is the procedure that was actually used by *Gan and Allen* [2002b, Figure 22] to calculate the terms displayed there. This procedure can give different results than the time average of the time series of terms from (A13) and (A14), mistakenly reported as the procedure followed by *Gan and Allen* [2002b, Figure 22]. The value of the sum $\langle \mathrm{ADV} \rangle$ is preserved using either method, but the partitioning into components $\langle \mathrm{ADVX} \rangle$ and $\langle \mathrm{ADVY} \rangle$ can be different.

Appendix B: Net Contributions to *apg*

[51] To aid in the interpretation of the ageostrophic pressure gradient term,

$$\mathrm{apg} = fU + P_y, \tag{B1}$$

from (1), we calculate the net contributions of fU and P_y to apg, following a procedure similar to that used in Appendix A for ADVX and ADVY in (A13) and (A14), respectively.

[52] For apg > 0, we define

$$\mathrm{Cor} = \frac{1}{2}(fU + |fU|) + \frac{1}{2}\left(P_y - |P_y|\right) \tag{B2}$$

$$\mathrm{pre} = \frac{1}{2}\left(P_y + |P_y|\right) + \frac{1}{2}(fU - |fU|). \tag{B3}$$

As a result, the sum

$$\mathrm{apg} = \mathrm{Cor} + \mathrm{pre} \tag{B4}$$

is preserved, but the common part of opposite sign that would cancel in the sum is removed. For apg < 0, (B2) and (B3) are altered by reversing the sign of the terms with absolute values.

[53] In Figure 11 we plot the spatial distribution of the terms in (1) time averaged over the 72 day time period 23 May to 2 August. The time average net contribution of pre to apg is calculated in the same manner described for calculating the net contributions of $\langle \mathrm{ADVX} \rangle$ and $\langle \mathrm{ADVY} \rangle$ to $\langle \mathrm{ADV} \rangle$ in Appendix A.

[54] **Acknowledgments.** This research was supported by the National Science Foundation Coastal Ocean Processes (CoOP) program under grant OCE-9907854. J. Gan is grateful to Hong Kong University of Science and Technology for additional support. The authors thank A. Huyer, A. Kurapov, and J. Barth for helpful discussions. Thoughtful comments from two anonymous reviewers are appreciated.

References

Barth, J. A., S. D. Pierce, and R. L. Smith (2000), A separating coastal upwelling jet at Cape Blanco, Oregon and its connection to the California Current System, *Deep Sea Res., Part II*, *47*, 783–810.

Barth, J. A., R. O'Malley, and A. Y. Erofeev (2003), SeaSoar observations during the Coastal Ocean Advances in Shelf Transport (COAST), Survey I: 23 May–13 June 2001, *Data Rep. 191*, Coll. of Oceanic and Atmos. Sci., Oreg. State Univ., Corvallis.

Blumberg, A. F., and G. L. Mellor (1987), A description of a three-dimensional coastal ocean circulation model, in *Three-Dimensional Coastal Ocean Models*, *Coastal Estuarine Ser.*, vol. 4, edited by N. Heaps, pp. XX–XX, AGU, Washington, D. C.

Boyd, T., M. D. Levine, P. M. Kosro, S. R. Gard, and W. Waldorf (2002), Observations from moorings on the Oregon Continental Shelf, May–August 2001, *Ref. 2002-6, Data Rep. 190*, Coll. of Oceanic and Atmos. Sci., Oreg. State Univ., Corvallis.

Castelao, R. M., and J. A. Barth (2005), Coastal ocean response to summer upwelling favorable winds in a region of alongshore bottom topography variations off Oregon, *J. Geophys. Res.*, *110*, C10S04, doi:10.1029/2004JC002409.

Gan, J. P., and J. S. Allen (2002a), A modeling study of shelf circulation off northern California in the region of the Coastal Ocean Dynamics Experiment: 1. Response to relaxation of upwelling winds, *J. Geophys. Res.*, *107*(C9), 3123, doi:10.1029/2000JC000768.

Gan, J. P., and J. S. Allen (2002b), A modeling study of shelf circulation off northern California in the region of the Coastal Ocean Dynamics Experiment: 2. Simulations and comparisons with observations, *J. Geophys. Res.*, *107*(C11), 3184, doi:10.1029/2001JC001190.

Gan, J. P., J. S. Allen, and R. Samelson (2005), On open boundary conditions for a limited-area coastal model off Oregon. Part 2: Response to wind forcing from regional mesoscale atmospheric model, *Ocean Modell.*, *8*, 155–173.

Kosro, P. M. (2005), On the spatial structure of coastal circulation off Newport, Oregon, during spring and summer 2001 in a region of varying shelf width, *J. Geophys. Res.*, doi:10.1029/2004JC002769, in press.

Kurapov, A. L., J. S. Allen, G. D. Egbert, R. N. Miller, P. M. Kosro, M. Levine, and T. Boyd (2005a), Distant effect of assimilation of moored currents into a model of coastal wind-driven circulation off Oregon, *J. Geophys. Res.*, *110*, C02022, doi:10.1029/2003JC002195.

Kurapov, A. L., J. S. Allen, G. Egbert, R. Miller, P. M. Kosro, M. D. Levine, T. Boyd, J. A. Barth, and J. N. Moum (2005b), Assimilation of moored velocity data in a model of coastal wind-driven circulation off Oregon: Multivariate capabilities, *J. Geophys. Res.*, *110*, C10S08, doi:10.1029/2004JC002493.

Large, W. G., and S. Pond (1981), Open ocean momentum flux measurements in moderate to strong winds, *J. Phys. Oceanogr.*, *11*, 324–336.

Mellor, G. L., and T. Yamada (1982), Development of a turbulence closure model for geophysical fluid problems, *Rev. Geophys.*, *20*, 851–875.

Oke, P. R., J. S. Allen, R. N. Miller, G. D. Egbert, J. A. Barth, T. J. Boyd, P. M. Kosro, and M. D. Levine (2002a), A modeling study of the three-dimensional continental shelf circulation off Oregon. Part I: Model-data comparisons, *J. Phys. Oceanogr.*, *32*, 1360–1382.

Oke, P. R., J. S. Allen, R. N. Miller, and G. D. Egbert (2002b), A modeling study of the three-dimensional continental shelf circulation off Oregon. Part II: Dynamical analysis, *J. Phys. Oceanogr.*, *32*, 1383–1403.

Samelson, R. M., P. Barbour, J. Barth, S. Bielli, T. Boyd, D. Chelton, P. Kosro, M. Levine, E. Skyllingstad, and J. Wilczak (2002), Wind stress forcing of the Oregon coastal ocean during the 1999 upwelling season, *J. Geophys. Res.*, *107*(C5), 3034, doi:10.1029/2001JC000900.

Spitz, Y. H., J. S. Allen, and J. Gan (2005), Modeling of ecosystem processes on the Oregon shelf during the 2001 summer upwelling, *J. Geophys. Res.*, doi:10.1029/2005JC002870, in press.

J. S. Allen, College of Oceanic and Atmospheric Sciences, Oregon State University, Corvallis, OR 97331-5504, USA. (jallen@coas.oregonstate.edu)

J. Gan, Department of Mathematics and Atmospheric, Marine and Coastal Environment Program, Hong Kong University of Science and Technology, Kowloon, Hong Kong. (magan@ust.hk)